

UC Riverside

UC Riverside Electronic Theses and Dissertations

Title

Complex Faulting in the Yuha Desert: Implications for Fault Interaction

Permalink

<https://escholarship.org/uc/item/4vp4z70z>

Author

Kroll, Kayla Ann

Publication Date

2012

Peer reviewed|Thesis/dissertation

UNIVERSITY OF CALIFORNIA
RIVERSIDE

Complex Faulting in the Yuha Desert: Implications for Fault Interaction

A Thesis submitted in partial satisfaction
of the requirements for the degree of

Master of Science

in

Geological Sciences

by

Kayla Ann Kroll

September 2012

Thesis Committee:

Dr. Gareth J. Funning, Chairperson
Dr. Elizabeth S. Cochran
Dr. Keith B. Richards-Dinger

Copyright by
Kayla Ann Kroll
2012

The Thesis of Kayla Ann Kroll is approved:

Committee Chairperson

University of California, Riverside

Acknowledgments

I am grateful to my advisor, Elizabeth Cochran, without whose help, support and understanding, I would not be here. I thank you, Elizabeth, for believing that I could be a good scientist, even if I didn't believe it myself. You taught me how to conduct a project from start to finish; from data collection to the publication. I truly appreciate all your time and effort. Thank you for being the kind of advisor I needed, for being tough on me, extending praise when I earned it, and for always expecting the highest quality. A special thanks for keeping me around, especially on the bad days; like when I deleted over 100,000 manual picks... twice.

I am deeply indebted to Keith Richards-Dinger, for always having all the answers! Thank you for the countless hours of conversation about code, parameter selection, error analysis and for always putting an equation to the completely qualitative explanations I had. You taught me how to compile decades old Fortran code, the basics about linear algebra, inverse theory, and the 'find' command, that saved my life. Thank you for taking over as the 'go - to' person for all my questions, and for always being willing to help. You are a great teacher and a brilliant scientist and I am better for having worked with you.

I would like to thank Gareth Funning, my new advisor. You have always held me to the highest of standards and have accepted nothing less. Through everything, you have always encouraged me to the best that I can be. I appreciate your extensive edits and attention to detail. Your effort helped make this thesis what it is, and for that, I will always be grateful.

I am incredibly appreciative of Danielle Sumy, whom I met less than one year ago, but has been incredibly influential to my career and my life. Not only have you been

a fantastic friend Danielle, but your overwhelming support and constant encouragement has helped me through the roughest of times. You brought back my sanity when I was convinced I was going crazy. You have introduced me to expert scientists, taught me everything you know, and let me learn from your experiences. Words can not express how grateful I am, or how lucky feel to have you in my life. Your continued support of my career advancement makes me truly believe that I can be a real scientist someday. You are awesome!

Lastly, to Jascha Polet, Chad Severson, and Harmony Colella. To Jascha, because if it wasn't for your encouragement (and your Intro to Seismology/Geophysics classes) I would never have considered this degree. You are a true proponent of each of your students and an incredible academic, two outstanding qualities not often found in one individual. Chad, you are the kindest, hardest working, most optimistic, light-hearted, and fun-loving person I have ever met. You bring out the best in people, and you make me want to be a better person. I can not begin to thank you enough for your support in the last two years, and especially for sitting by my desk through kinematic modeling. Harmony, thank you for being so honest and a great friend. I genuinely appreciate all that you have contributed to my education and to my life.

Dedication

I dedicate this work to the four people in my life that have made this journey possible. First to my Mother; whose strength inspires me, whose dedication drives me, whose ambition motivates me, and whose work ethic and perfection were instilled in me. Thank you Mom for teaching me, I love you dearly. To Deborah Ann; for your constant, unequivocal support. For continuing to believe in me, for always being positive, helping mold me into the woman I am today, and putting me in my place when I deserved it. To Jara; for being my person, for being the better part of me, and for being the bestest friend in the whole wide world. I could never ask for a better friend than you. Lastly, to Marchelle; for teaching me patience and how to love unconditionally. To my family, I thank you.

ABSTRACT OF THE THESIS

Complex Faulting in the Yuha Desert: Implications for Fault Interaction

by

Kayla Ann Kroll

Master of Science, Graduate Program in Geological Sciences
University of California, Riverside, September 2012
Dr. Gareth J. Funning, Chairperson

We determine precise hypocentral locations for over 3,600 aftershocks that occurred in the Yuha Desert region following the 4 April 2010 M_w 7.2 El Mayor-Cucapah (EMC) earthquake until 14 June 2010 through a series of absolute and relative relocation procedures with algorithms including *hypoinverse*, *velest* and *hypoDD*. Location errors were reduced to ~ 20 m horizontally and ~ 80 m vertically. The locations reveal a complex pattern of faulting with *en echelon* fault segments trending in toward the northwest, approximately parallel to the North American-Pacific plate boundary and *en echelon*, conjugate features trending to the northeast. The relocated seismicity is highly correlated with the mapped faults that show triggered surface slip in response to the EMC mainshock. Aftershocks are located between depths of 2 km and 11 km, consistent with previous studies of seismogenic thickness in the region. Three-dimensional analysis reveals individual and intersecting fault planes between 5 km and 10 km in the along-strike and along-dip directions. These fault planes remain distinct structures at depth, indicative of conjugate faulting, and do not appear to coalesce onto a through-going fault segment. Measurements of surface displacement along the Laguna Salada-West and East (LS-W and LS-E, respectively) branches reveal no triggered surface creep on

either branch following the EMC mainshock. Approximately 2 mm of triggered surface creep was observed on the LS-W in response to the 14 June 2010 M5.7 Ocotillo earthquake, however no creep was measured along the LS-E. Relocated seismicity shows that aftershock activity occurs along the LS-E, however not along the LS-W in the time period between these earthquakes. We observe a complex spatiotemporal migration of aftershocks, with the area east of the LS-W only becoming seismically active following the EMC mainshock. Aftershock activity abruptly shuts off in this area following the Ocotillo earthquake. The majority of seismicity in the two-year period following the Ocotillo earthquake occurred along the LS-W, suggesting a complex spatial and temporal distribution of aftershock activity. The conjugate pattern of faulting, combination of seismicity and triggered surface creep and non-uniform aftershock migration patterns suggest that strain in the Yuha Desert is being accommodated in a complex manner.

Contents

List of Figures	x
List of Tables	xv
0.1 Introduction	1
0.2 Geologic Setting	4
0.3 El Mayor-Cucapah Mainshock	6
0.4 Data	7
0.5 Relocation Procedure and Results	7
0.5.1 Data Gathering and Pre-processing	9
0.5.2 Computing Absolute Locations with <i>Hypoinverse</i>	10
0.5.2.1 <i>Hypoinverse Background and Processing</i>	10
0.5.2.2 <i>Hypoinverse Results (H1a Locations)</i>	11
0.5.3 Improving the Velocity Structure Using <i>Velest</i>	12
0.5.3.1 <i>Velest Background</i>	12
0.5.3.2 <i>Velest Procedure</i>	13
0.5.3.3 <i>Velest Results and Absolute Locations (H1b Locations)</i>	14
0.5.4 Using <i>HypoDD</i> for Relative Relocation	16
0.5.4.1 <i>HypoDD Background</i>	16
0.5.4.2 <i>HypoDD Procedure: Manual Arrivals (H2a Locations)</i>	17
0.5.4.3 <i>HypoDD Results: Manual Arrivals (H2a Locations)</i>	18
0.5.4.4 <i>HypoDD Background: Cross – Correlation</i>	18
0.5.4.5 <i>HypoDD Procedure: Cross–Correlations and Manual Arrivals (H2b Locations)</i>	19
0.5.4.6 <i>HypoDD Results: Cross–Correlations and Manual Arrivals (H2b Locations)</i>	20
0.6 Fault Interaction	21
0.6.1 Seismicity Correlates with Mapped Triggered Surface Slip	22
0.6.2 Persistence of Individual Fault Planes with Depth	23
0.6.3 Alternating Stick-slip and Creep on the Branches of the Laguna Salada Fault	25
0.6.4 Non-uniform Expansion of the Aftershock Distribution	26
0.7 Discussion and Conclusions	28
A	63
B	67

List of Figures

0.1	<p>Seismicity of the Yuha Desert in the 30 years before the 4 April 2010 M_w 7.2 EMC earthquake. Studies completed in the Yuha Desert region prior to the EMC earthquake were minimal. The Laguna Salada fault (LSF) as mapped following the 1892 M7.2 earthquake and associated faults are shown in black [17] and the faults mapped in by [39] in northern Baja California and through the Yuha Desert are shown as white dotted lines, LS-W - Laguna Salada - west branch, LS-E - Laguna Salada - east branch, LR - Lucy Ridge, PSH - Palm Springs Hill. Additionally, minimal seismicity was recorded in this area before this earthquake. Thirty years of seismicity in the Yuha Desert ($\sim 3,500$ earthquakes) prior to the El Mayor-Cucapah earthquake relocated by [31] are shown by the blue dots. Inset map shows location of the EMC mainshock (yellow star) and the prominent faults surrounding the Imperial Valley region, southern California; ESF - Elsinore Fault, SJF - San Jacinto Fault, IF - Imperial Fault and LSF - Laguna Salada Fault. The red box denotes the region expanded in the main figure.</p>	32
0.2	<p>Map and cross-sectional views of positive and negative flower structures. Both systems show imbricate fault structure at the surface, where individual fault planes merge onto a single throughgoing structure at depth. Left: Positive flower structures are typically associated with uplifted antiforms created in transpressional environments dominated by reverse faulting. Right: Negative flower structures are typically seen in transtensional wrench settings dominated by normal offsets.</p>	33

0.3	Details of the EMC mainshock. Increased seismicity (blue diamonds) was evident in the geothermal and surrounding areas in March 2010. 15 foreshocks (red circles) occurred in the 24 hours preceding the mainshock. The first mainshock subevent occurred at the epicenter (yellow star), and ruptured with normal and dextral motion towards the southeast. A second larger subevent occurred 15 seconds later, and ruptured from the epicenter towards the international border, also with normal and dextral motion [33]. The EMC sequence has a combined moment magnitude of M_w 7.2. This event ruptured ~ 120 km of crust in a complex fashion. Surface rupture, south east of the epicenter (blue line) has been inferred from InSAR data and image cross-correlation [89]. [16] mapped the surface rupture northwest of the epicenter (red lines). Rupture to the northwest occurred in an complicated manner, which included rupture jumping across several fault strands through the Sierra-Cucapah mountain range. Triggered surface slip in the Yuha Desert, mapped by [67] is shown by the pink lines. Additional surface rupture from the 1892 $\sim M7.1$ event was mapped by [17] and is shown by the thick black lines, and southern California faults are shown grey.	34
0.4	A) Aftershocks recorded by the SCSN (blue dots) through of 6 April 2010. Two main aftershock clusters formed within the two days following the mainshock, one in the southeast near the epicenter (yellow star) and the second in the Yuha Desert region, north of the international border. B) An enlarged picture (red box from Figure 4A), showing earthquakes that occurred in the Yuha Desert region following the EMC and before the installation of the UC-RAMP stations (triangles) on 6 April 2010. This area is of particular interest as there are no known through-going fault structures mapped between the Laguna Salada fault in the south and the Elsinore fault in the north.	35
0.5	An enlarged picture (red box from Figure 4A), showing the events that occurred in the Yuha Desert region during the UC-RAMP deployment period. The study area (outlined by the grey box) contains 4,323 events that are listed in the SCSN catalog. Here, we relocate these events using <i>hypoDD</i> [88] and they are used to further asses the fault structure in this area. The relocated seismicity will help determine how strain is accommodated in a region where a through-going plate boundary can not be defined.	36
0.6	Flow chart of the data processing scheme that was used in this analysis. The resulting location codes (i.e. <i>HIa</i> , <i>HIb</i> , <i>HDa</i> , and <i>HDb</i>) are color coded according to the color of their corresponding locations as shown in Figure 0.9 (<i>HIa</i>) , Figure 0.11 (<i>HIa</i> and <i>HIb</i>), and Figure 0.13 (<i>HIb</i> and <i>HDb</i>).	37
0.7	Top: Histogram of differences between manual and automatic phase arrival picks. Negative values represent waveforms for which an automatic pick was made before a manual pick. Bottom: Diagram showing the difference in automatic (red line) versus manual (green line) P-wave picks on three of five SCSN stations used in this study. The offset between automatic and manual picks range drastically, between 0 s and 3.0 sec, with a median offset of 0.1289 sec. An arrival misidentified by 0.1 sec can lead to location differences of approximately 1km.	38

0.8	<p><i>A priori</i> (<i>crust0</i>) velocity model used in the initial absolute location determination with <i>hypoinverse</i>. This velocity model was modified from the SCEC Community Velocity Model, version 4 (CVM-v4) for the Imperial Valley region (SCEDC, 2012: http://www.data.scec.org/research-tools/3d-velocity.html). We reduced the velocities between the surface and 5 km depth based on a linear interpolation to accommodate the surface sediment layers and reduce the number of air-quakes (e.g. earthquakes that relocate above the Earth's surface) produced through <i>hypoinverse</i>.</p>	39
0.9	<p>Comparison of the first round of relocations with the original SCSN catalog locations. Over 4,300 aftershocks were recorded and located in the Yuha Desert by the SCSN between 6 April and 14 June 2010 (grey dots). P- and S-wave phase arrivals were manually identified for these events and absolute locations were calculated with <i>hypoinverse</i> [43] with a modified version of CMV-v4 Imperial Valley input velocity model (<i>HIa</i> locations shown by the purple dots) (Figure 0.8). Horizontal and vertical absolute location errors were reduced to 1.5 km and 2.3 km, respectively. RMS timing errors are reduced to 0.25 sec.</p>	40
0.10	<p>Results of the <i>velest</i> inversion. Top: The UC-RAMP and 5 SCSN stations used in the inversion are plotted as a function of station correction. The non-uniform distribution of fast and slow station corrections suggest a complicated velocity structure in the Yuha Desert, with many small scale heterogeneities. Faults in green were mapped by [39], faults shown in black were mapped by [17] and those in blue were mapped following the EMC mainshock by [67]. Bottom: The best fitting velocity model (<i>crust1</i>) for our station and event distribution that resulted from the <i>velest</i> joint inversion. The inversion was completed with the Quality A events from the <i>HIa</i> location analysis (see Table 0.1 and Figure 0.9). The inset table lists the associated station corrections.</p>	41
0.11	<p>Comparison of improved (<i>HIb</i>) locations with initial <i>hypoinverse</i> locations (<i>HIa</i>) (Figure 0.9). The resulting locations (<i>HIa</i> locations) from the initial run through <i>hypoinverse</i> were separated into quality bins based on RMS residuals (See Table 0.2). The Quality A events were used in a joint inversion analysis to determine station corrections (<i>sta1</i>) and a best-fitting velocity model (<i>crust1</i>) with the <i>velest</i> algorithm. The <i>sta1</i> and <i>crust1</i> results along with the manual phase picks were incorporated into <i>hypoinverse</i>. Horizontal and vertical location errors were reduced to 0.5 km and 1.8 km, respectively. The RMS residual was reduced to 0.13 sec. The <i>HIb</i> locations were used as the starting locations in the double-difference relative relocation analysis with <i>hypoDD</i> [88].</p>	42
0.12	<p>Three empirically-derived linear relationships between correlation coefficient and <i>a priori</i> weight assignment for P-waves and S-waves. Events with correlation coefficients below 0.7 have been severely down-weighted (red curve), while events with CC values between 0.7 and 0.8 have only been slightly down-weighted (teal curve). Events with the most similarity (i.e. CC greater than 0.8) retain their CC value (blue curve).</p>	43

0.13	Comparison between the absolute locations (<i>HTb</i>) and the relative locations (<i>HDb</i>). The resulting locations (<i>HDb</i> locations) from the double-difference relative relocation are shown in the red dots. The <i>crust1</i> velocity model, manual phase arrivals and cross-correlation delay times were used in this analysis. The initial locations used in this step (shown in the teal dots) are the <i>HTb</i> absolute locations displayed in Figure 0.11. Relative location errors were estimated to be ~ 20 m horizontally and ~ 80 m vertically through a bootstrap analysis. The RMS timing errors were reduced to 0.004 s.	44
0.14	The relocated aftershocks that occurred between 6 April and 14 June 2010 are shown by the red dots. Faults mapped in blue were observed to have triggered surface slip following the EMC earthquake [67]. The majority of the seismicity occurred east of the LS-W. The seismicity correlates well with the mapped fault structure of the Yuha Desert. Lineations of seismicity are seen along the right-lateral, northwest trending LS-E branch, along left-lateral northeast trending faults in the Yuha Well Fault Zone, and the Yuha Fault. Inverted black triangles indicate a point along the surface projection of the inferred fault plane shown in cross-section in Figure 0.15.	45
0.15	Three-dimensional cross-sectional views where seismicity is highly correlated with mapped faults showing triggered surface slip. Left: A prominent fault of the Yuha Well Fault Zone is correlated with relocated seismicity (red dots) that forms a nearly vertical plane (heavy dashed line). The inferred plane dips $\sim 89^\circ$ SE and projects to the surface (shown by inverted black triangles in Figure 0.14 at the approximately location of the fault mapped by [67]). Right: Seismicity highlighting the LS-E (red dots) correlates well with the projection of the fault to the surface (heavy dashed line). The inferred subsurface extension of the LS-E dips $\sim 85^\circ$ NE. 46	46
0.16	Comparison between the mapped triggered surface slip [67], relocated seismicity and data collected from two creepmeters installed along the LS-W and LS-E. Top: Red dots indicate the relocated seismicity, plotted along with the fault structure in the Yuha Desert area. The green and yellow circles along the LS-W and LS-E branches, respectively, represent the two creepmeters installed in the area. The LS-W creepmeter was installed 10 April 2010, while the LS-E creepmeter was not installed until 14 August 2010. Bottom: Creepmeter time series (data courtesy of Roger Bilham, 2012) show ~ 2 mm of surface creep on the LS-W occurring coincident with the M5.7 Ocotillo earthquake. While the LS-E creepmeter was not installed during this event, surface displacement was not observed in the precise caliper measurements taken along this fault segment.	47

0.17	Comparison of aftershocks that occurred in response to the EMC mainshock (red dots) and the Ocotillo earthquake (blue dots). The aftershocks plotted in red occurred between 6 April and 14 June 2010, the two month period between the EMC and Ocotillo events. The locations shown in red are relocated in this work. The aftershocks plotted in blue were relocated by [31], and occurred after the Ocotillo earthquake. This temporal plot shows that the LS-E is seismicity active before the Ocotillo event, however it shuts down and seismicity transfers to the LS-W. Surface creep was not seen on the LS-E following either earthquake; however, the LS-W was observed to creep ~ 2 mm in response to the Ocotillo earthquake. Additionally, the seismicity that occurred following the Ocotillo earthquake appears to form a connection between the LS-W and LS-E on an unmapped fault segment (indicated by the arrow and highlighted by the orange dashed line).	48
0.18	Relocated seismicity plotted as a function of time after the EMC mainshock. A non-uniform expansion of aftershock activity is seen following the mainshock. Some areas are active early, namely the south of the Yuha Well fault and one of the en echelon northeast trending segments of Yuha Well Fault Zone. Additional early activity forms a northwest trending band adjacent to the LS-E. Activity in the areas that show seismic deformation shortly after the EMC mainshock, become relatively inactive, or shut off completely. After ~ 40 days, the majority of deformation is accommodated along the LS-E and in the Yuha Well Fault Zone.	49

List of Tables

0.1	Seismic sensors used in this study; also shown in Figure 4b. CI = SCSN network code, ZY = UC-RAMP network code. EH[Z,N,E] sensors are short period, strong motion accelerometers, HN[Z,N,E] are weak motion sensors, BH[Z,N,E] components are continuous broadband, HH[Z,N,E] are triggered high-broadband, and the HN[Z,N,E] sensor at WES is a triggered high broadband accelerometer. The component codes Z, N, E represent the vertical, north (horizontal) and east (horizontal) directions respectively. The ‘*’ indicates the sensor that was used in this study, when multiple sensors were available. The sample rate is only reported for the sensors used in this study.	8
0.2	Aftershocks were divided into bins based on data quality defined by the RMS residual. The joint inversion for the optimal 1D velocity model and station corrections that best represent the station configuration and event distribution was performed with the Quality A earthquakes. Quality B through D event bins were used to test the stability of the best-fitting velocity model and station corrections.	13

0.1 Introduction

In areas where there are no continuous fault structures, secondary faults may accommodate strain in a complex manner. Stress changes induced by moderate to large earthquakes can trigger aftershocks on these secondary faults, particularly in zones where the primary fault plane is obscured by geometric complexities, bends, or discontinuities [66, 71]. Aftershock activity has also been shown to increase in regions of concentrated stress, such as those formed at the ends of primary faults [9, 77, 50, 41]. The 4 April 2010 M_w 7.2 El Mayor-Cucapah (EMC) earthquake produced a vigorous cloud of aftershocks in the Yuha Desert region north of the U.S.-Mexico international border, 30 km west of Calexico, California approximately 4 km NW of the mainshock rupture termination. In the Yuha Desert, complex faulting has been observed in the area between the Elsinore Fault in the northwest and the Laguna Salada fault toward the south-southeast, where through-going fault structures have not been identified. Precise aftershock locations enable the examination of the intricate network of faults seen in the Yuha Desert region.

Prior to the EMC mainshock, limited geological or geophysical work had been done in the Yuha Desert region. Previous studies show geologic evidence for complex faulting [10, 39] in two primary orientations. [39] observed northwest trending right-lateral and northeast trending left-lateral strike-slip faults, with sporadic north-south trending faults displaying normal offset (Figure 0.1). The Laguna Salada fault exhibits anastomosing behavior in the Yuha Desert region, bifurcating 1 km south of the border into the Laguna Salada West (LSW) and the Laguna Salada East (LSE) branches [39]. [31] relocate the sparse number of earthquakes in the region from 1981 through 2010 (Figure 1). Seismicity was generally distributed in isolated clusters along northwest trending faults near the mapped trace of the LS-W. Two linear north/northeast trend-

ing features are observed in the background seismicity to the NE of the LS-E branch (Figure 0.1).

Previous studies suggest that complex surface faulting may become simpler at depth as faults coalesce onto prominent structures [90, 5, 89]. Active flower structures have been observed along major strike-slip fault systems such as the southern San Andreas fault [90], along other major strike-slip fault systems in southern California. [25, 26, 13] and along the North Anatolian fault [5]. [24, 25, 26, 27] describe flower structures as being a significant feature of strike-slip fault zones. Positive flower structures are typically associated with uplifted antiforms, in a transpressional wrench fault system dominated by reverse separations (Figure 0.2). Negative flower structures are seen in transtensional wrench environments, with faults displaying predominantly normal offsets (e.g. San Andreas Fault zone near Mecca Hills [13]) (Figure 0.2). Conversely, it has also been shown that highly active, immature strike-slip fault systems may consist of parallel through-going fault strands, with secondary splays at varying orientations [66, 71, 62]. The San Jacinto fault zone is a prime example, where it has been shown with geologic and geophysical data that fault strands do not coalesce with depth [72]. This work aims to examine whether the fault structure changes with depth in the Yuha Desert region. We examine the three dimensional characteristics of seismicity to determine whether the complex fault structure seen at the surface by [39] and [67] coalesce onto simpler, primary structures at depth.

Aftershock distributions can illuminate areas of complex faulting surrounding approximately contiguous mainshock fault planes. For example, [30] showed that aftershocks following the 1999 Hector Mine event occurred along a set of complex, conjugate faults with both strike-slip and dip-slip motion, but whose orientations were consistent with the regional stress field. Additionally, both observational [75] and theoretical stud-

ies (i.e. [2] and [47]) suggest a change in slip behavior, with alternating shallow creep and stick-slip behavior on adjacent fault segments, within complex fault zones. While other faults in the area (i.e. the Superstition Hills, Elmore Ranch, and Imperial faults) have been known to exhibit shallow surface creep [22, 3, 37, 49, 45, 89], previous studies have not attributed mapped surface offsets to creep along any of the faults in the Yuha Desert region. Detailed study of the aftershock distribution may pertain to the investigation of the possible trade-off between seismicity and shallow creep in the area.

The spatio-temporal distribution of aftershock sequences provides a number of general observations about stress changes induced by a large mainshock [55, 41, 82], aftershock rates and migration patterns [11, 34], and post seismic deformation [35, 56], to name a few. Several studies have shown increased aftershock activity on the fault around patches of high slip and high moment release [83, 80, 46]. Others have shown higher aftershock rates in areas with increased shear and Coulomb stress at the ends of a fault rupture [50, 82]. [19] showed that these zones of increased stress become spatially heterogeneous along faults with complex geometries or step-overs, with higher aftershock activity in step-over and branching regions [61, 64]. Expansion of aftershocks, away from the epicenter with time has been observed and may indicate post-seismic deformation and afterslip [57, 36, 56]. [79] and [92] attribute the expansion of the aftershock zone to non-uniform stress changes due to the mainshock. [11] demonstrates a similar effect with the rate- and state-dependent friction laws and attributes the majority of the expansion to the non-uniform (in both space and time) stress change following an instantaneous stress increase/decrease. Here, we describe the spatio-temporal distribution of aftershocks within the Yuha Desert region, and discuss the relationship to changes in stress, aftershock expansion patterns, and post-seismic deformation.

The work presented here involves the relocation of aftershock hypocenters through a series of absolute and relative relocation steps using the *hypoinverse* [43], *velost* [42] and *hypoDD* [88]. We compare the relocated seismicity with the EMC surface offsets mapped by [67] and with faults previously mapped by [10] and [39] where surface slip was not observed following the EMC. We examine the fault structure at depth in the Yuha Desert to determine whether the complex faulting seen at the surface extends to depth. Additionally, we investigate the spatio-temporal distribution of events within the region to identify any migration patterns that may be evident within the seismicity. Furthermore, we explore the possibility of shallow surface creep accompanying the stick-slip behavior seen in the Yuha Desert and discuss future work associated with this dataset.

0.2 Geologic Setting

The Yuha Desert lies within a region of complex faulting between the Laguna Salada Fault zone to the south and Elsinore Fault zone to the north (Figure 0.1). Regionally, this area is located west of the termination of the San Andreas Fault and North American-Pacific plate boundary, in the Salton Trough region. Previous studies in Baja California suggest that the Laguna Salada fault system initiated after the formation of the San Andreas Fault during a period of late Quaternary wrench deformation [8, 12, 51, 58, 39]. These authors report primarily right-lateral strike-slip motion with a smaller component of normal slip along the Laguna Salada Fault extending from the Sierra Cucapah range, northwestward toward the US-Mexico border.

Farther north, work has been done in California studying the Elsinore Fault. Owing to the location, northwest orientation, and slip rate of the Elsinore fault, some

authors suggest that this is the northward extension of the Laguna Salada fault [e.g. [20, 52, 48]]. Along its northern extent, the Elsinore fault is mapped as a fairly simple, single strand, whereas in the south it splays into two strands, the Elsinore fault to the west and the Agua Tibia Earthquake Valley (ATEV) fault to the east [48]. Slip is partitioned between these two fault strands with slip rate estimates of 5 to 6 mm/yr on the Elsinore and 0.5 to 2.8 mm/yr on the ATEV faults [48]. The Elsinore fault is mapped further south, past the Coyote Mountains, ~5 km northwest of the Yuha Desert [67]. Seismicity indicates that the seismogenic depth of the fault zone decreases toward the south along the Elsinore, with depths of ~17 km in the north and ~10 km in the south, due to a steeper geothermal gradient as extension in the Salton trough is approached. [48].

Anastomosing behavior of the Laguna Salada faults is described by [39] in the Yuha Desert and Laguna Salada valley region (Figure 0.1), and occurs both north and south of the USMexico border. Three strands of the Laguna Salada fault exist south of the international border. The first strand extends from the southwest border of Lucy Ridge (Figure 0.1), trending 105° . In the Pinto Wash area, north of the border, the fault bends northward and bifurcates. This zone is referred to by [67] as the LS-W, with one strand trending 140° and the other 150° . The LS-E trends $160^\circ - 170^\circ$, directly through the region being studied here. [39] also mapped multiple horsetail fractures at the northern end of the LS-E branch. All branches of the Laguna Salada dip steeply to the west at angles between 52° and 90° . [39] reports that the Yuha Desert is underlain by folded, tilted and faulted strata of the Palm Springs formation. This work also describes a complex system of folds with axes trending dominantly toward the northeast, and rotating clockwise approaching the Laguna Salada Fault zone. [67] suggest that shallow faults in this area are bounded by these structures.

0.3 El Mayor-Cucapah Mainshock

The 4 April 2010 M_w 7.2 El Mayor-Cucapah (EMC) earthquake ruptured multiple fault strands within a complex plate boundary zone (Figure 0.3) [33]. The epicenter was located in an area that connects the major right-lateral strike-slip fault system in the Salton Trough region (San Andreas, San Jacinto, and Elsinore faults) to the spreading center regime in the Gulf of California [89]. The EMC is thought to be the largest earthquake on this section of the North American-Pacific plate boundary zone since an earthquake on 23 February 1892, estimated to be greater than M_w 7.1 with 22 km of dextral-oblique rupture [17]. According to [33] and [89], a smaller, normal faulting event preceded the mainshock by 15 seconds. The mainshock ruptured bilaterally, ~ 55 km to the southeast toward the Gulf of California with mostly dextral strike-slip motion, and ~ 65 km northwestward on multiple fault segments with both normal (east-side down) and dextral motion. The northwestward rupture propagation ceased ~ 5 km south of the US-Mexico international border [67]. [16] mapped ~ 120 km of surface rupture in the Baja California region and report up to ~ 2.5 m of right-lateral surface slip. Remote-sensing techniques also reveal an average of ~ 2 m of right-lateral surface slip in this area and slip inversions revealed up to 6 m of slip along the fault planes [89]. Triggered fault slip was documented in the Salton Trough (e.g. Coyote Creek Fault, Superstition Hills Fault and Imperial Fault as well as the Mecca Hills segment of the San Andreas Fault) and surrounding regions including the Yuha Desert (primarily along the LS-W and LS-E, Yuha Well Fault and Yuha Well Fault Zone), 60 km–172 km north of the epicenter, by [67].

0.4 Data

In order to better constrain aftershock locations in the Yuha Desert, an array of eight temporary stations was installed as part of the University of California Rapid Aftershock Mobilization Project (UC-RAMP) to supplement the existing permanent Southern California Seismic Network (SCSN) where coverage was limited (Figure 0.4). The eight stations (COON, MLDN, OCCM, OYSB, PNT0, SHCM, USG, and WAGN) of the UC-RAMP network included six portable REFTEK and two Quanterra 330 recording systems with eight L4 sensors (weak motion), seven episensors (strong motion), and one FBA23 sensor. The US-RAMP network was installed at the surface above one of the two main clusters of aftershocks from the EMC earthquake (Figure 0.4). During the two-month deployment, the Southern California Seismic Network (SCSN) reported 4,323 aftershocks (Figure 0.5) within the 20 km by 14 km study area (32.63°N , -115.95°E to 32.73°N , -115.75°E). The SCSN near the Yuha Desert consists of 5 short period stations (COK, CRR, SGL, and YUH) and one continuous broadband site (WES) with multiple channels. Table 0.1 contains more information about the sensors used in this study.

0.5 Relocation Procedure and Results

Routine earthquake locations generated by regional seismic networks are generally based on phase arrivals manually identified by an analyst. Following large earthquakes, however, seismic networks often become inundated with aftershock activity, making manual phase picking too laborious and time consuming to be completed in real time. Therefore, in these situations, it is common for locations to be derived based upon automatically detected phase arrivals, which increase location errors [83, 73, 4].

Station Name	Network	Component	Sample Rate (sps)
COK	CI	EHZ	100
CRR	CI	EHZ	100
SGL	CI	EHZ	100
WES	CI	BH[Z,N,E]*, HH[Z,N,E], HN[Z,N,E]	40
YUH	CI	EHZ	100
COON	ZY	EH[Z,N,E]* HN[Z,N,E]	200
MLDN	ZY	EH[Z,N,E]* HN[Z,N,E]	100
OCCM	ZY	EH[Z,N,E]* HN[Z,N,E]	100
OYSB	ZY	EH[Z,N,E]* HN[Z,N,E]	100
PNT0	ZY	EH[Z,N,E]* HN[Z,N,E]	100
SHCM	ZY	EH[Z,N,E]* HN[Z,N,E]	100
USG	ZY	EH[Z,N,E]* HN[Z,N,E]	100
WAGN	ZY	EH[Z,N,E]* HN[Z,N,E]	100

Table 0.1: Seismic sensors used in this study; also shown in Figure 4b. CI = SCSN network code, ZY = UC-RAMP network code. EH[Z,N,E] sensors are short period, strong motion accelerometers, HN[Z,N,E] are weak motion sensors, BH[Z,N,E] components are continuous broadband, HH[Z,N,E] are triggered high-broadband, and the HN[Z,N,E] sensor at WES is a triggered high broadband accelerometer. The component codes Z, N, E represent the vertical, north (horizontal) and east (horizontal) directions respectively. The ‘*’ indicates the sensor that was used in this study, when multiple sensors were available. The sample rate is only reported for the sensors used in this study.

The Southern California Seismic Network (SCSN) detected and located 4,323 aftershocks from 6 April 2010 (following the EMC earthquake) through 14 June 2010 (the final day of the UC-RAMP deployment) within the 20 km by 14 km study area using primarily automatically detected phase arrivals and a layered 1D velocity model to locate the events with *hypoinverse* [43]. The velocity model used is similar to the [23] velocity model for southern California (e.g. [83, 73, 84, 74, 32, 38]). Horizontal and vertical location errors and root mean square (RMS) travel time residual of these events

in the SCSN catalog are 1.89 km, 2.59 km, and 0.36 sec, respectively. Location errors are known to be larger in this area of the Imperial Valley because strong velocity heterogeneities arise due to deep sedimentary units [20, 74, 32]. Additional uncertainty in earthquake locations in the Yuha Desert is attributed to inadequate azimuthal station coverage along the edge of the SCSN.

In this study, we undertake a relocation analysis of seismic events in the SCSN catalog to accurately characterize the fault structure of the Yuha Desert. Analytical techniques include: 1) manual picking of the P- and S-wave arrivals, 2) association of phase arrivals with individual event origins and locations, 3) determination of the best-fitting 1D velocity model with associated station corrections for the distribution of stations and events, and 4) relocation of event hypocenters by analysis of closely spaced event pairs. A flow chart of the complete data processing steps is shown in Figure 0.6.

0.5.1 Data Gathering and Pre-processing

We first manually identify P- and S-wave arrivals on the vertical (Z) and horizontal (N/E) components of all 13 stations, respectively. In general, the accuracy of manually identify phase arrivals is greater than that of an automatic pick. The top panel in Figure 0.7 shows a histogram of timing difference automatic and manually identified picks, and the bottom panel shows an example of the average offset between the two. For this dataset, the automatic picks ranged from 0 sec to ~ 3.0 sec difference when compared to manual picks for the same event. Waveforms from the SCSN stations were obtained via the Seismogram Transfer Program (STP) from the Southern California Earthquake Datacenter. One-minute waveform records were cut from the continuous database starting at the event origin times given in the SCSN catalog. For consistency, all S-wave picks made based upon the first arrival on either horizontal component. Be-

fore processing, we removed the mean and bandpass filtered the waveforms between 1 and 15 Hz.

0.5.2 Computing Absolute Locations with *Hypoinverse*

0.5.2.1 *Hypoinverse Background and Processing*

These absolute phase arrivals were then used in the *hypoinverse* algorithm to locate events [43]. For the first set of iterations, the P-wave and S-wave picks are weighted 100% and 75%, respectively, since the S-wave are often less accurate than P-wave picks and can often be obscured by the P-wave coda. For these iterations, we modified a 12-layer 1D starting velocity model (*crust0*) from the SCEC Community Velocity Model version 4 for the Imperial Valley region (Figure 0.8). We use a V_p/V_s ratio of 1.68, calculated specifically for the Yuha Desert using Wadati diagrams [40, 18] for 100 events. The starting or ‘trial location of each event was placed beneath the station with the first arrival at 7 km depth. The hypocenters are allowed to freely deviate from the trial location, within the constraints of the damping parameters (default values used here). The trial location is adjusted through a least-squares iterative approach until the minimum residual between the observed and predicted travel-times is reached. Predicted travel times are determined with ray tracing from the source to each station with the initial velocity model.

To estimate the hypocentral error, *hypoinverse* computes the variance matrix, which is derived from the matrix containing the partial derivatives of the travel-time with respect to changes in the hypocenter location. The 4x4 covariance matrix containing the hypocentral parameters (x, y, and z) plus the origin time (t) is subdivided into the 3x3 submatrix containing only the spatial coordinates and rotated into the principal component coordinate system of the hypocentral solution. Standard errors are calcu-

lated by taking the square roots of the eigenvalues of the 3x3 covariance submatrix. These standard errors correspond to the 32% confidence ellipsoid interval (i.e. the true hypocenter has a 32% likelihood of lying within the ellipsoid defined by the eigenvalues and eigenvectors of the covariance matrix). The 32% confidence ellipsoid is the 2σ error ellipsoid in three dimensions. The standard errors should be multiplied by a factor of 2.4 to achieve the 95% confidence ellipsoid. Additionally, to correctly account for systematic (i.e. velocity structure) and random (i.e. picking) errors, the covariance matrix can be weighted with the ERCOF (the coefficient of the RMS travel-time residual) and ERR (e.g. assumed reading and timing error) parameters within *hypoinverse*, respectively, prior to the inversion process [43]. For cases where the velocity model is known with confidence (i.e. estimated through a joint-inversion process) and where picking errors are reduced by manual picking, these parameters can be down-weighted significantly. In our analysis, these parameters were given full weight, therefore the likelihood of the true hypocenter lying within the error ellipsoid defined by the covariance matrix is likely greater than 32%, however still less than 95% since we did not multiply our results by 2.4. *Hypoinverse* reports vertical errors as the projection of the longest principal axis onto a vertical line running through the hypocenter, and horizontal errors as the length of the longest principal axis, as viewed from above, and projected onto a horizontal plane [43].

0.5.2.2 *Hypoinverse* Results (*HIa* Locations)

The resulting locations for 4,073 earthquakes (hereinafter referred to as the ‘*HIa*’ locations) are shown in Figure 0.9. The absolute horizontal and vertical location errors of the *HIa* locations were reduced to 1.59 km and 2.3 km, respectively, with a RMS residual of 0.25 s. This represents only a marginal improvement over the original

SCSN locations (i.e. 1.89 km horizontally, 2.8 km vertically, and RMS of 0.36 s). The majority of the improvement is seen in the vertical error and RMS residual, which we attribute to better S-wave arrival picks and a slightly improved velocity model. When comparing the two sets of locations (i.e. original SCEC locations shown by the grey dots, and the *H1a* locations shown by the purple dots in Figure 0.9) the *H1a* locations form a tighter cluster which is shifted approximately ~ 1 km to the northeast, which is an effect of the velocity model. These locations remain cloud-like; therefore, identification of fine-scale fault features is impossible. These locations can be improved by employing a velocity structure appropriate for the station and event distribution and a set of station terms that accounts shallow velocity heterogeneities as we show below.

0.5.3 Improving the Velocity Structure Using *VelEst*

0.5.3.1 *VelEst* Background

To improve the absolute locations initially calculated for each event with hypoinverse, we use the joint hypocenter inversion algorithm, *velEst*, [42] to determine the best-fitting 1D velocity model and station corrections for the distribution of stations and events. Station corrections can account for near-surface velocity structure beneath the station without the use of a 3D velocity model. Seismic wave travel-times contain information about both the earthquake location and the velocities of the materials between the source and the seismometer that waves propagate through. A joint inverse problem is one where two unknowns (e.g. the velocity and hypocentral model parameters) are varied to reduce the RMS residual. *VelEst* is a proven technique for 1D velocity model determination with local and regional arrays (e.g. [6, 76, 54, 59, 86, 78]) and, thus, is the preferred method to use in the Yuha Desert.

0.5.3.2 *Velest Procedure*

A hierarchical analysis of the seismicity catalog to find the best-fitting model and station corrections is employed by [42, 76, 59, 78]. In our work, we adopt this method and begin by subdividing our *H1a* results from *hypoinverse* into categories based on the RMS residual. The first simultaneous inversion for hypocenters, velocity, and model and station corrections focuses on 420 events that meet the most stringent RMS residual cutoff (RMS residual ≤ 0.12 s). We classify these events as ‘Quality A events, and further partition the remaining $\sim 3,600$ events into Quality B through D categories by relaxing the RMS residual cutoff (Table 0.2).

Quality Bin	Min RMS (s)	Max RMS (s)	Total # of events
A	0	0.12	420
B	0.13	0.17	1,942
C	0.18	0.23	1,536
D	0.24	1	157

Table 0.2: Aftershocks were divided into bins based on data quality defined by the RMS residual. The joint inversion for the optimal 1D velocity model and station corrections that best represent the station configuration and event distribution was performed with the Quality A earthquakes. Quality B through D event bins were used to test the stability of the best-fitting velocity model and station corrections.

Before beginning the inversion process, we relocate the Quality A events in the single-event mode (SEM) of *velest*, which only inverts for new locations based on an *a priori* (*crust0*) velocity model. We incorporate this step to verify that the initial locations are not significantly different compared to the *H1a* locations before starting the joint inversion (simultaneous mode) procedure. With new initial locations for the Quality A events, we perform the joint inversion in simultaneous mode (SIM), which outputs a modified velocity model (*crustA*), station corrections (*staA*), and refined hypocenters. Lastly, the Quality A events are run through SEM with *crustA* and *staA* to verify location improvement. All parameters were left at default values in the inversion,

except for using the V_p/V_s ratio we measured specifically for the Yuha Desert. A detailed explanation of all parameters is given in the *velest* users manual [42]. As *velest* is a code specifically written and tested on local networks and events, the default parameters were relevant for this study. Quality B, C, and D event bins are then added to the Quality A bin sequentially, and the joint inversion process is completed again, each time incorporating the results from the previous step. Small perturbations to the input velocity model and station corrections are made until RMS residuals, velocity model, and station terms stabilize. For example, the addition of erroneous layers (i.e. 200 km depth) and inappropriately high or low velocities (15 km/s or 0.5 km/s, respectively) should be removed in the output, e.g. the optimal 1D velocity model. In total, four velocity models (*crustA – D*) and four sets of station corrections (*staA – D*) were determined, where each new model is a modification of the previous one, until the best-fitting velocity model is achieved. Since *velest* does not compute the covariance matrix, the location errors cannot be accurately assessed in this step; therefore, the *crust1* and *sta1* data (Figure 0.10) and absolute travel times are again used in *hypoinverse*.

0.5.3.3 *Velest Results and Absolute Locations (H1b Locations)*

The *velest* processing step results in a best-fitting velocity model (*crust1* 10 layer model) and set of station corrections (*sta1*) for the available station distribution and observed earthquakes. The *crust1* velocity model closely resembles the results of a refraction study completed by [20], as it includes very low seismic velocities for the upper 3 km of sediments. The thirteen stations (five SCSN and eight UC-RAMP stations) are plotted to show the station delay times (Figure 0.10). From previous studies that involve the use of static station terms (e.g. [63]), we might expect nearby stations to have similar station terms. In general, station corrections are positive (i.e. faster) for

soft rock or sedimentary sites and negative (i.e. slower) for bedrock or basement sites. Figure 0.10 shows a sporadic pattern of the station terms with most sites being negative with respect to reference station, MLDN. Station terms for sites closest MLDN vary from 0.17 s at OCCM to -0.22 s at SHCM. Farther west of OCCM, the term at site YUH flips back to -0.17 s. East of SHCM, station terms at the PNT0 and SGL sites reduce to -0.12 s and -0.15 s, respectively. As the SHCM station was installed near the bedrock of Signal Hill, this result was expected. The non-uniform distribution of fast and slow station delays suggests that the length scale of the velocity heterogeneity in the Yuha Desert is quite small, as is supported by the complex geology detailed by [39].

A second iteration of absolute location determination with *hypoinverse* is required in order to accurately estimate the hypocentral errors associated with the locations. In this step, the absolute arrival times derived from manual picking were combined with the *crust1* velocity model and *sta1* set of station corrections to invert for absolute locations (labeled *H1b* in Figure 0.11). After the *hypoinverse* and *velest* procedures, the resulting hypocenters have absolute horizontal and vertical location errors of 0.55 km and 1.8km, respectively, with a RMS residual of 0.13 s. At this stage in the earthquake relocation process, the aftershocks begin to ‘collapse into linear features resembling faults. These features appear to trend predominantly toward the northwest, with smaller features trending northeast. The most prominent NW striking feature lies slightly east, but parallel to the LS-E. Obvious NE striking features lie at the northwestern end of the mapped extensions of the LS-E and LS-W faults. In a 3D view, planar features that trend northwest parallel to the LS-E and toward the northeast can both be identified. Aftershocks in the area north and between stations MLDN and SGL have begun to collapse slightly when compared to the *H1a* locations; however, it is still difficult to discern clear linear or planar features within the distribution of seismicity.

Seismicity at this point in the relocation process is still cloud-like and does not form sharp lineations, even after incorporating the best-fitting 1D velocity model and station terms. To further improve the results, we use the *H1b* hypocenter results and *crust1* velocity model were used as input in the relative relocation process.

0.5.4 Using *HypoDD* for Relative Relocation

0.5.4.1 *HypoDD* Background

To improve the resolution of the *H1b* locations, we employ the double difference algorithm, *hypoDD* [88]. *HypoDD* refines the event locations through an iterative least-squares approach that reduces the differential travel-time residual between pairs of events recorded at a common station. *HypoDD* takes advantage of the assumption that rays from a closely spaced pair of events to a common station travel along similar paths; therefore, the travel-time difference between the pair at a common station is due to the spatial offset between the two earthquakes. This assumption is valid, provided that the event-pair separation distance is small compared to the length scale of the velocity heterogeneities. The algorithm then iteratively adjusts the vector distance between the event-pair to reduce the double-difference travel-time residual, resulting in a ‘relative’ location of the event-pair. The term ‘relative’ simply implies that each event is located relative to its closest neighbors. This approach is not sensitive to the absolute location of the event in three-dimensional space; therefore, appropriate steps, such as the *hypoinverse* and *veltest* procedures described above, must be taken before beginning the relative relocation process. As an example, running *hypoDD* with an inappropriate velocity model tends to push the location of the entire cluster of events in a direction related to the type of velocity perturbation (i.e. for an overly fast velocity model, the cluster gets pushed farther away from the array). In these situations, the

relative location of one event compared to its neighbors remains unaffected, but the absolute errors can change dramatically.

HypoDD incorporates both differential travel-time and up-sampled cross-correlation delay time data, individually or combined. [88] demonstrate how increasing the number and type of observations used can reduce location error. They begin with only P-wave travel-time data and then add S-wave travel-time data; finally, they combine the P- and S-wave travel times with P- and S-wave cross-correlation delay times to arrive at the best-fitting hypocenter. One critical feature of the algorithm is the complex weighting and reweighting scheme. While the actual weighting values are specific to a given problem, it is generally suggested that for the initial iterations the cross-correlation data should be down-weighted compared to the travel-time data (hereinafter referred to as ‘catalog data’) and up-weighted in later iterations. The idea is that the catalog data help constrain the absolute hypocentral locations at a regional-scale, while the cross-correlation data help constrain the hypocentral location relative to an event’s neighbors. Each event’s neighbors are selected prior to the relocation in a preprocessing step based on a set of user-defined parameters. *HypoDD* can be further tailored to the event and station distribution in a specific region by adjusting a variety of parameters. For a detailed description of the most important input parameters, see Appendix A.

0.5.4.2 *HypoDD Procedure: Manual Arrivals (HDa Locations)*

In our relative relocation procedure, the first round of processing incorporates manually-picked P- and S-wave arrival times, the *crust1* velocity model, the previously determined $V_p/V_s = 1.68$, and the *H1b* results as starting locations. Based upon our small station and event distribution, we search for the 10 closest neighbors within a 2 km radius for each event, where each event must be recorded by a minimum of 4 stations.

This process resulted in 227,942 P- and 147,178 S-phase differential times. During relocation, P-and S-wave phases that did not meet residual and event-pair separation distance cutoffs were down-weighted. The residual and event-pair separation distance cutoffs were also decreased after every second iteration. Residual and distance cutoffs decrease from 8 s to 4 s and 6 km to 3 km, respectively, over 4 sets of 2 iterations.

0.5.4.3 *HypoDD Results: Manual Arrivals (**HDa** Locations)*

For the 3,655 events relocated (labeled **HDa** in the flow chart in Figure 0.6) in this step, 83% of the original pick data was preserved and the RMS residual was reduced to 0.018 s. Mean horizontal and vertical errors were estimated to be ~ 130 m and ~ 360 m, respectively, through a bootstrap test. Three-dimensional visual inspection shows that the northwest and northeast trending features that were just visible in the hypoinverse results persist here. These earthquakes appear to cluster in linear and planar, rather than cloud-like, structures shown in the **HIb** results (Figure 0.11).

0.5.4.4 *HypoDD Background: Cross – Correlation*

It is widely accepted that using delay times derived from cross-correlating waveforms for a pair of earthquakes recorded by a common station increases the precision of the relative event locations [14, 69]. [14] attribute this effect to the improved precision of the up-sampled cross-correlation delay times versus manually picked arrivals. Manually identifying phase arrivals can reduce timing errors from 0.1 s - 0.3 s typical of automatically detected arrivals to 0.1 s in the optimal case. Timing errors of automatically detected arrivals are primarily due to the high SNR ratios, emergent nature of some phases and coda (particularly in the case of S-wave arrivals of local events) [88]. Manual phase picking can reduce hypocentral errors from ~ 1 km to several hundred meters in

the horizontal direction. Vertical hypocentral errors can be up to two times larger due to the difficulty in identifying the S-wave arrival, either by eye or using an automatic detection algorithm [69]. The precision of the manually picked arrival is affected by random errors associated with human reading [73, 70]. Furthermore, S-wave arrivals may not be accurately identified, thus proving poor depth constraint. Employing waveform cross-correlation techniques has been proven to aid in the reduction of both horizontal and vertical hypocentral errors of 1-2 orders of magnitude [60, 21, 65, 85, 68]. Cross-correlations take advantage of the similarity of approximately co-located events and up-sampled waveforms to increase the precision of the arrival time. Additionally, since arrival times determined by cross-correlations only require the correlation window to be centered on a packet of energy, S-wave arrivals can be more readily identified even in the case of an emergent arrival or in the presence of P-wave coda. Up-sampled cross-correlation delay times can thus reduce the timing errors to 0.001 s, which translates to hypocentral errors as small as tens to hundreds of meters. The number of correlations is dependent on the number of events, stations, phases and components considered $[N*(N-1)*S*Ph*C/2]$; where N = number of events, S = number of stations, Ph = number of phases, and C = number of components], so the number of correlations performed can increase very rapidly ($> 10^9$ calculations). We minimize the number of calculations and the amount of computing time needed to run the cross-correlations by restricting the number of correlating events (or neighbors).

0.5.4.5 *HypoDD Procedure: Cross-Correlations and Manual Arrivals (**HDb** Locations)*

We limit the number of computations needed to determine cross-correlation delay times by assuming that events with large event-pair separation distances (i.e. $>$

~ 1 km) travel along significantly different ray paths and will, therefore, have dissimilar waveforms. Starting from the ***HD*b**** locations, we determine the 20 closest neighbors within a 1 km volume for each target event to use in the cross-correlation procedure. Nearly 4 million cross-correlations were performed for P- and S-wave phases on the vertical and north components of the 13 stations, respectively. A 0.8 second window is used for both phases; however, we center the window on the P-wave arrival (i.e. 0.4 s before and after the arrival), but use a smaller waveform segment before the S-wave arrival (0.2 s) to avoid correlating P-wave coda. The cross-correlation delay times are weighted based on the correlation coefficient and an empirically derived weighting scheme (Figure 0.12). Only event pairs with cross-correlation coefficients higher than 0.7 are retained.

0.5.4.6 *HypoDD Results: Cross-Correlations and Manual Arrivals (***HD*b**** Locations)*

The final relocation step combines the manually picked travel times (230,337 P-phase and 148,412 S-phase differential times), 304,963 P-phase and 157,702 S-phase cross-correlation delay times, the *crust1* velocity model, and the ***HD*a**** locations. The relative relocation errors of ~ 20 m horizontally and ~ 80 m vertically are estimated with a bootstrap method. The final locations (***HD*b****) are shown in Figure 0.13 and the hypocentral locations and origin times can be found in the electronic supplement of this paper. These results are consistent with the relocations of southern California seismicity completed by [31]. Aftershocks occur as shallow as ~ 3 km depth, consistent with the refraction study of [20] who show that sedimentary units in the Imperial Valley and surrounding region extend to depths between 3 and 4 km. Seismicity reaches maximum depths of ~ 11 km, consistent with the suggested seismogenic depth of the crust to the northwest, also derived from seismicity [48].

Seismicity resulting from the final relocation step are no longer cloud-like and do, indeed show structure. In map view, linear bands of seismicity trend toward the northwest, with conjugate bands striking toward the northeast (Figure 0.14). We compare the relocated seismicity with triggered surface slip mapped by [67] and find clear agreement between the seismicity and mapped, northeast-trending faults in the Yuha Well Fault Zone and the Yuha fault. Additionally, aftershocks align along the eastern branch of the northwest-trending LS-E fault. Several smaller northwest and northeast-trending lineations are also discernable in the seismicity, which do not appear to be associated with faults mapped by [67], particularly the NE trending band of seismicity to the NW of the Yuha Well fault and smaller NW trending bands toward the east and parallel to the LS-E. In three-dimensional cross-sections, relocated seismicity forms distinct planar features. For example, *en echelon* faulting of the Yuha Well Fault Zone persists at depth on individual fault planes with approximately vertical dips (Figure 0.15), where we plot events within 250 m on either side of the faults projection to the Earths surface. The seismicity here highlights planes that are small ($< \sim 5\text{km}$) in both the along-strike and along-dip directions. In many cases (e.g. LS-E and along the Yuha Well Fault Zone) the plane highlighted by the seismicity projects to the surface and correlates well with mapped faults. Additionally, the seismicity adjacent to the LS-E appears to be steeply dipping towards the NE (Figure 0.15), and separated from nearby events, suggesting that it is not connected to neighboring faults at depth.

0.6 Fault Interaction

We relocated over 3,600 aftershocks that occurred in the Yuha Desert following the EMC earthquake during the 2-month deployment period of the UC-RAMP tempo-

rary network of seismographs. We manually identified over 110,000 P- and S- wave phase arrivals, calculated absolute locations and inverted for the minimum 1D velocity model with *hypoinverse* and *velest*, respectively. Precise relative locations were found using a 1D velocity model, differential travel times, and cross-correlation delay times with *hypoDD*. The resulting earthquake locations permit the investigation of tectonic processes in the fault step-over region between the Elsinore and Laguna Salada faults. The following sections explore how faults interact and strain is accommodated in the Yuha Desert region.

0.6.1 Seismicity Correlates with Mapped Triggered Surface Slip

The final relative relocations are plotted along with the faults that were observed to have slipped at the surface at the time of the EMC earthquake by [67] in Figure 0.14. Faults in the Yuha Desert display a variety of kinematic behavior, including conjugate right and left-lateral motion, as well as normal motion [67]. The Yuha Well fault (unmapped prior to the EMC) is a northeast striking fault located between stations PNT0 and MLDN toward the southeast of the study area that experienced nearly 50 mm of left-lateral surface-slip, and the *en echelon* left-lateral faults of the Yuha Well Fault Zone toward the northwest of the study area slipped as much as 19 mm [67]. The northwest striking LS-E and LS-W segments branches both demonstrated ~ 40 mm of right-lateral slip in addition to a small normal component of ~ 2 mm on each fault. Interestingly, the LS-E branch showed east-side up extensional motion, while the LS-W showed west-side up motion, creating a down-dropped graben between the segments. [67] note they only map faults that exhibited obvious, recent surface slip related to the EMC earthquake; although, several previously mapped active fault strands were noted, but not recorded during their field surveys.

A visual inspection indicates a correlation between the mapped fault structure [67] and seismicity. Relocated aftershocks appear to collapse onto linear features trending to the northeast both in the NW and SE of the study area. Additionally, earthquakes are clustered in lineations oriented toward the northwest along the LS-E segment and ~ 2.5 km east of the LS-E. These prominent features in the seismicity strongly correlate with mapped faults that exhibited the greatest amount of surface slip [67]. Relocated seismicity highlights both the mapped northwest trending right-lateral faults and northeast trending left-lateral faults. Several smaller northwest and northeast-trending lineations are also discernable in the seismicity, which do not appear to be associated with faults mapped by [67]. This suggests that some slip was accommodated by fault planes that only slipped at depth in the Yuha Desert, in addition to the faults that slipped at the surface. Further investigation of the aftershock focal mechanisms will verify the fault kinematics at depth, as well potentially illuminate the importance of any normal faulting in the area.

0.6.2 Persistence of Individual Fault Planes with Depth

Geological investigations require a significant amount of interpretation, as the structure mapped at the surface must be extrapolated to depth. Combining the results of geologic field mapping with precisely located earthquakes enables the joint investigation of the fault structure. A variety of fault structures, including flower structures (e.g. where complex surface faults coalesce onto simpler structures at depth) and conjugate faulting (e.g. where complex surface faults remain individual planes at depth) have been identified along major strike-slip faults.

[90] and [25, 26] note active flower structures along the San Andreas fault and other prominent strike-slip faults in southern California; while [30] and [72] suggest that conjugate faulting is common in highly active, immature fault systems.

If faults merge at depth, a flower structure may be highlighted by the seismicity where complex imbricate surface faulting coalesces onto a through-going plane at depth. Generally, displacement along the *en echelon* sub-parallel segments occurs in the same direction (i.e. all right-lateral or all left-lateral). Traditionally, flower structures are seen along mature fault systems near areas of geometric complexity. In the case of the EMC earthquake, [89] suggest the InSAR, image correlation and GPS data of the mainshock can be modeled well by using simple fault planes, lacking much geometric complexity. Alternatively, [30] show a complex set of conjugate faults in the Lavic Lake region of the Hector Mine mainshock from relocated aftershocks. Here, faults extend to depth as individual, cross cutting fault strands where northern trending faults demonstrate right-lateral slip while the conjugate faults experience left-lateral motion.

A three-dimensional analysis of the relocated seismicity reveals multiple, clear planar fault features. Evident planar features such as those of the Yuha Well Fault zone show *en echelon* behavior at depth, mirroring what is seen on the surface. The seismicity adjacent to the LS-E forms a steeply dipping, planar feature that is divided from the neighboring earthquakes. Figure 0.15 shows cross-sections of the Yuha Well Fault Zone and the LS-E where the fault plane, inferred from the seismicity, projects to the Earth's surface in approximately the same location as the fault mapped by [67] and indicated by the black inverted triangles in Figure 0.14. In the area southeast of the Yuha Well Fault Zone and east of the LS-E it is possible to discern intersecting fault planes, however these planes do not merge onto a single structure. Based on the relocated aftershocks presented in this study there is no indication of a larger, through-

going fault segment suggestive of a flower structure. The complex, unconnected fault structure in this small dataset is, however, consistent with a complex set of conjugate faults along an immature fault system similar to that shown by [30] showed in the relocated aftershocks that occurred in the Lavic Lake region of the faults that ruptured during the Hector Mine earthquake. A 3D video of our relocated seismicity plotted with depth is provided as an electronic supplement to this work (Appendix A).

0.6.3 Alternating Stick-slip and Creep on the Branches of the Laguna Salada Fault

Several faults in Southern California that make up the plate boundary system north of the EMC mainshock rupture, such as the Superstition Hills, Elmore Ranch, and Imperial faults have been shown to creep ([22, 3, 37, 49, 45]); however, creep had never been previously documented along faults in the Yuha Desert. Two creepmeters were installed along the LS-W (10 April 2010) and LS-E (August 2010) faults following the EMC mainshock to investigate the behavior of the major faults within the Yuha Desert [67]. Figure 0.16a shows the locations of the relocated seismicity, the mapped faults, and the creepmeters. The data from the creepmeters are plotted in Figure 0.16b (personal communication; Bilham, 2012). Here, we see no continuous creep following the EMC earthquake; although, ~ 2 mm of triggered creep along the LS-W segment was coincident with a M5.7 earthquake that occurred on 14 June 2010 near the town of Ocotillo, California (Figure 0.16b). The LS-W branch was not seismically active during the 2-month period leading up to this aftershock; however, [31] show that this fault segment experiences a vigorous aftershock sequence following the Ocotillo earthquake (Figure 0.17). Caliper measurements ($10 \mu\text{m}$ precision) were made along the LS-E on 12 May 2010 and again before the installation of the creepmeter in August 2010, which

showed no surface offset [67]. Field measurements along the LS-E following the EMC earthquake and Ocotillo event show no triggered creep, nor does the creepmeter show any continuous creep. In contrast to the LS-W, the LS-E is very seismically active in the 2-month period following the EMC event. [31] show not only that the LS-E, but the entire Yuha Desert east of the LS-W dramatically decreases in seismic activity following the Ocotillo earthquake. This suggests that fault slip behavior varies dramatically within the Yuha Desert; for example, certain faults show triggered creep (LS-W), while others exhibit stick-slip behavior (LS-E).

0.6.4 Non-uniform Expansion of the Aftershock Distribution

The spatio-temporal distribution of aftershock sequences can provide information about stress changes induced by a large mainshock [81], aftershock rates and migration patterns [11, 34], postseismic deformation and/or afterslip [56], fluid migration [53], and other phenomena. Several studies have shown increased aftershock activity in areas of high slip and high moment release (e.g. [83, 80, 46]). Others have shown higher aftershock rates in areas with increased shear and Coulomb stress at the ends of a fault rupture (i.e. [50, 82]). [19, 61, 64] showed that these zones of increased stress become spatially heterogeneous along faults with complex geometries or step-overs, with higher aftershock activity in step-over and branching regions. Other studies of expansion of aftershocks away from the epicenter with time suggest post-seismic deformation and/or afterslip as possible mechanisms [57, 56, 36, 7]. [79] and [92] attribute the expansion of the aftershock zone to non-uniform failure strength or post-seismic creep, respectively. [11] demonstrates a similar effect with the rate- and state- dependent friction laws and attributes the majority of the expansion to the non-uniform stress change and time-dependent nucleation following a stress step.

We plot the relocated aftershocks as a function of time following the EMC mainshock in Figure 0.18. Studies of typical aftershock sequences show a migration of activity away from the mainshock epicenter through time (e.g. [79, 56]). The distribution of aftershocks in this small area of the Yuha Desert does not show an expansion away from the epicenter with time. The epicenter of the mainshock is located toward the southeast, so the early events might be expected to occur in the SE while the later events would occur in the NW. Instead the early aftershocks are dispersed throughout the relatively small study region, but in two main groups, one in the southeast by the Yuha Well Fault and another cluster in the northwest along faults within the Yuha Well Fault Zone. Later events tend to align mostly along the LS-E branch, as well as the NE trending faults of the Yuha Well Fault Zone. Examining the seismicity in more detail shows one northeast trending fault of the Yuha Well Fault Zone is active early while two strands on either side of that fault become active later in the deployment period. Additionally, some areas are moderately active for a while, and then they shut off, almost completely. For instance, seismicity ceases in the area surround the Yuha Well Fault after ~ 35 days following the EMC earthquake. Alternatively, the LS-E branch only becomes active after this period (~ 35 days following the EMC earthquake) and remains active for the duration of the study (67 days following the EMC earthquake). While it is outside the scope of this paper, it is worth mentioning that the LS-W branch remains inactive until the Ocotillo earthquake on 14 June 2010, while the eastern Yuha Desert shows productive seismic activity. Following the Ocotillo earthquake, activity reverses and the eastern Yuha Desert shows little seismicity, while the majority of the seismicity is aligned along the LS-W branch. This behavior continues at least until 30 June 2011, the last day of seismicity relocated by [31].

0.7 Discussion and Conclusions

In summary, we relocate ~ 3600 aftershocks in the Yuha Desert region during the 2-month temporary deployment period of the UC-RAMP stations following the EMC earthquake on 4 April 2010. Using 420 of the best-located events, we employ a hierarchical analysis to invert for the best-fitting 1D velocity model and corresponding station corrections for our station and event distribution with *veltest* [42]. We apply the double-difference relative relocation algorithm, *hypoDD* [88], with the refined velocity model to further improve the hypocentral locations and obtain a high-resolution image of the seismic deformation in the Yuha Desert. Absolute location errors were reduced in *hypoinverse* to ~ 0.5 km horizontally, ~ 1.8 km vertically, with RMS timing errors of 0.25 s. This process results in relative location errors of ~ 20 m horizontally and ~ 80 m vertically, with RMS residuals of 0.004 s estimated through a bootstrap analysis. Depths of the events relocated through the *hypoDD* double-difference analysis are between 2 km and 11 km, consistent with previous studies [48] of the southern Elsinore fault.

We find that the relocated seismicity falls along right-lateral northwest and left-lateral northeast trending conjugate faults structures within the Yuha Desert and correlates well with the mapped faults that exhibit triggered surface slip as mapped by [67]. The pattern of aftershocks in three dimensions shows that these features appear to remain as distinct individual structures at depth, revealing a complex patchwork of conjugate faults. Conjugate faulting is supported by the orientation of faulting (i.e. strike of NW and NE trending fault structures separated by $\sim 35^\circ$ to 60°) and the variability in the sense of displacement (i.e. left-lateral motion on the northeast trending Yuha Well Fault and in the Yuha Well Fault Zone and right-lateral/normal motion on the northwest trending LS-W and LS-E [67]). The complex fault structure, minimal fault-

induced topographic expression, and variable slip direction (i.e. right- and left-lateral slip) is indicative of a fault system that has not accommodated much total strain. This is additionally supported by the low slip rates (up to 5 mm/yr) on the southern Elsinore [48] and northern Laguna Salada (~ 3 mm/yr) [52] faults. The Yuha Desert experienced less than 3,200 recorded earthquakes in the 30 years prior to the EMC earthquake which further supports the idea of minimal strain accumulation.

It has been shown, both observationally [1, 91, 16] and in dynamic models [15, 44, 29, 28] that large earthquakes can rupture multiple fault segments, negotiate geometric complexities, and jump large fault step-overs. [16] showed that the EMC mainshock rupture jumped an ~ 11 km extension step-over. The ability for rupture to jump a fault step-over is limited by several factors including step-over width, transpressional versus transtensional settings, and the presence of a linking segment [15, 44]. Rupture propagation is surely complicated by the addition of complex faulting within the step-over region. In the case of the EMC earthquake, rupture ceased ~ 4 km south-east of the Yuha Desert (the step-over region between the Elsinore and Laguna Salada faults) where an intricate patchwork of conjugate faults is seen. It is possible that the EMC rupture might have ended in the area because there was no single fault strand large enough to support the continuation of the rupture. We suggest that the fault pattern in the Yuha Desert acted as a barrier to rupture, inhibiting the EMC earthquake from jumping onto larger fault traces to the north and driving strain to be accommodated along smaller, adjacent fault segments.

The main trace of the Laguna Salada fault that last ruptured in the M7.2 1892 earthquake, splits into the LS-W and LS-E branches, only ~ 5 km south of the Yuha Desert. The parallel, NW trending branches experience a component of right-lateral and normal displacement, and are separated by a maximum of ~ 4 km at the surface [39, 67].

Both faults are reported to dip at the surface between 75° and 90° to the west [39]. If the dip becomes shallower with depth this could indicate that these traces are connected and may be governed by a single, through-going strand at depth. Examination of the distribution of seismicity along each branch with depth suggests the possibility of a connection of these structures. Seismicity on the LS-E occurs only during the period between the EMC and Ocotillo earthquakes (~ 9 May and 14 June 2010) at depths between 3 km and 11 km, and appears to be constrained on a vertical to subvertical east-dipping plane. Seismic events only occur along the LS-W following the Ocotillo aftershock, at depths between 2 km and 11 km, on approximately vertical to subvertical west-dipping plane. It is interesting to note a possible unmapped linking fault segment between the LS-W and LS-E highlighted by seismicity following the Ocotillo event (black dashed line in Figure 0.17). While the seismicity suggests that the main strands of the LS-W and LS-E are dipping subvertically away from each other and, therefore, may not merge onto a through-going fault at depth, they may, perhaps, be linked together by an unmapped fault segment.

In conclusion, we find that the relocated seismicity supports the complex pattern of faulting seen at the surface in the Yuha Desert. Furthermore, the rheology of the material in the Yuha Desert supports triggered aseismic creep in the west along the LS-W, at least at the surface, and stick-slip failure east of the LS-W. Lastly, aftershock activity induced by the EMC mainshock, east of the LS-W ceases after the Ocotillo earthquake, giving rise to prolonged seismic activity to the west. Due to the complex nature of faulting, the combination of triggered creep and stick-slip motion, and owing to its location in the step-over region between the Laguna Salada and Elsinore faults, several further investigations of the Yuha Desert are warranted. These studies include Coulomb stress transfer modeling, rupture propagation modeling through step-over regions with complex fault structures, and 3D and spatio-temporal analysis of the seismicity relocated in this study combined with the results of [31].

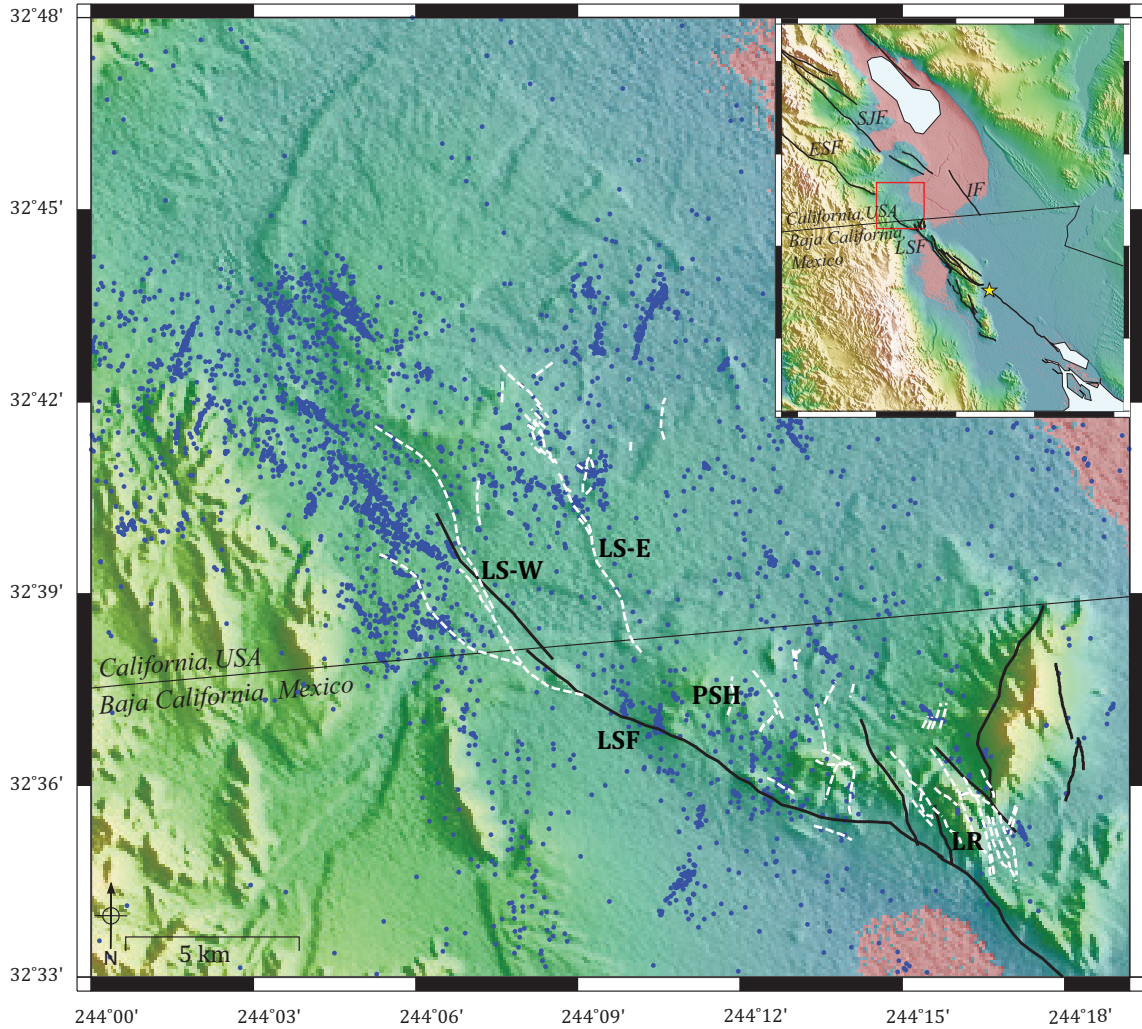


Figure 0.1: Seismicity of the Yuha Desert in the 30 years before the 4 April 2010 M_w 7.2 EMC earthquake. Studies completed in the Yuha Desert region prior to the EMC earthquake were minimal. The Laguna Salada fault (LSF) as mapped following the 1892 M7.2 earthquake and associated faults are shown in black [17] and the faults mapped in by [39] in northern Baja California and through the Yuha Desert are shown as white dotted lines, LS-W - Laguna Salada - west branch, LS-E - Laguna Salada - east branch, LR - Lucy Ridge, PSH - Palm Springs Hill. Additionally, minimal seismicity was recorded in this area before this earthquake. Thirty years of seismicity in the Yuha Desert ($\sim 3,500$ earthquakes) prior to the El Mayor-Cucapah earthquake relocated by [31] are shown by the blue dots. Inset map shows location of the EMC mainshock (yellow star) and the prominent faults surrounding the Imperial Valley region, southern California; ESF - Elsinore Fault, SJF - San Jacinto Fault, IF - Imperial Fault and LSF - Laguna Salada Fault. The red box denotes the region expanded in the main figure.

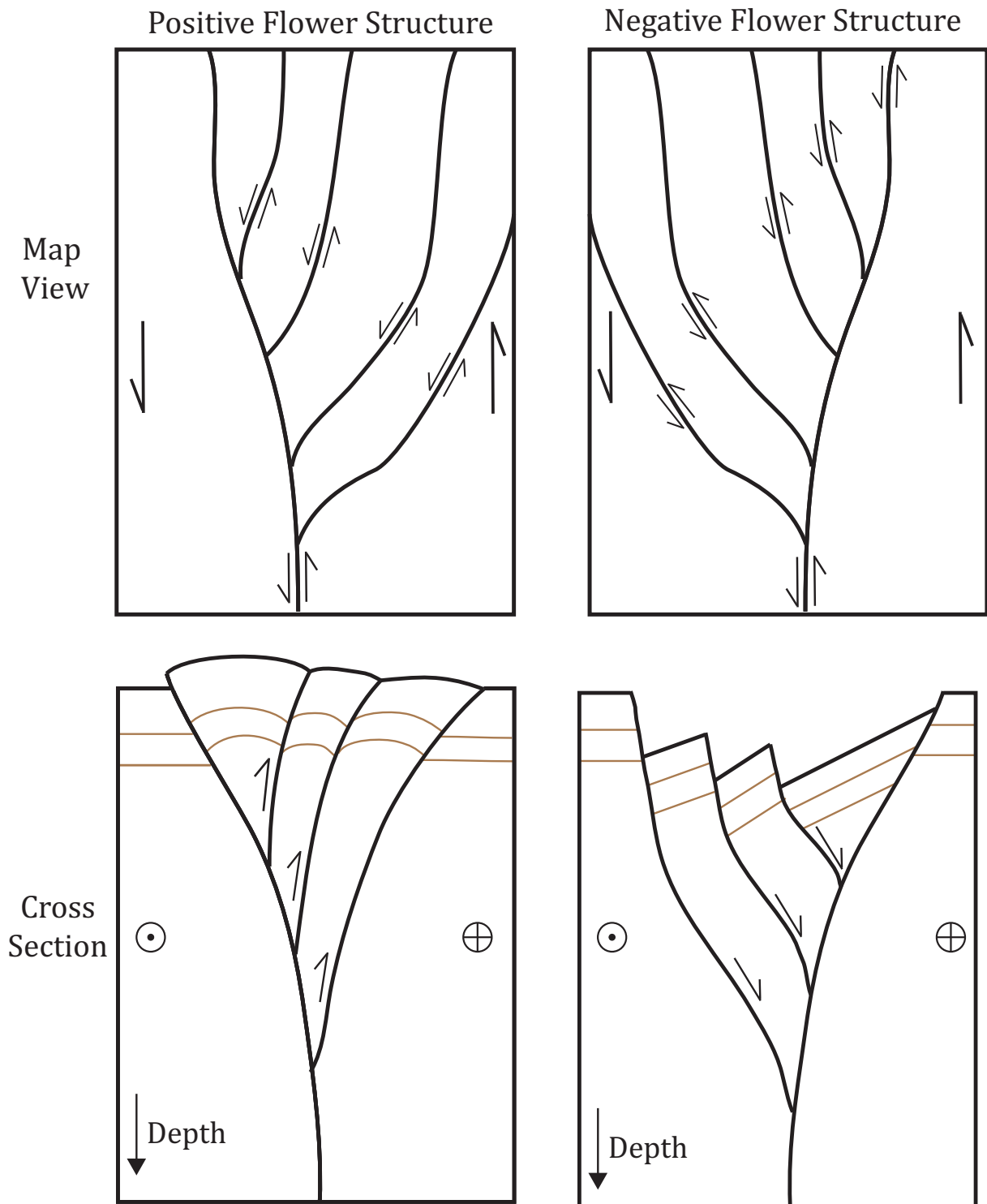


Figure 0.2: Map and cross-sectional views of positive and negative flower structures. Both systems show imbricate fault structure at the surface, where individual fault planes merge onto a single throughgoing structure at depth. Left: Positive flower structures are typically associated with uplifted antiforms created in transpressional environments dominated by reverse faulting. Right: Negative flower structures are typically seen in transtensional wrench settings dominated by normal offsets.

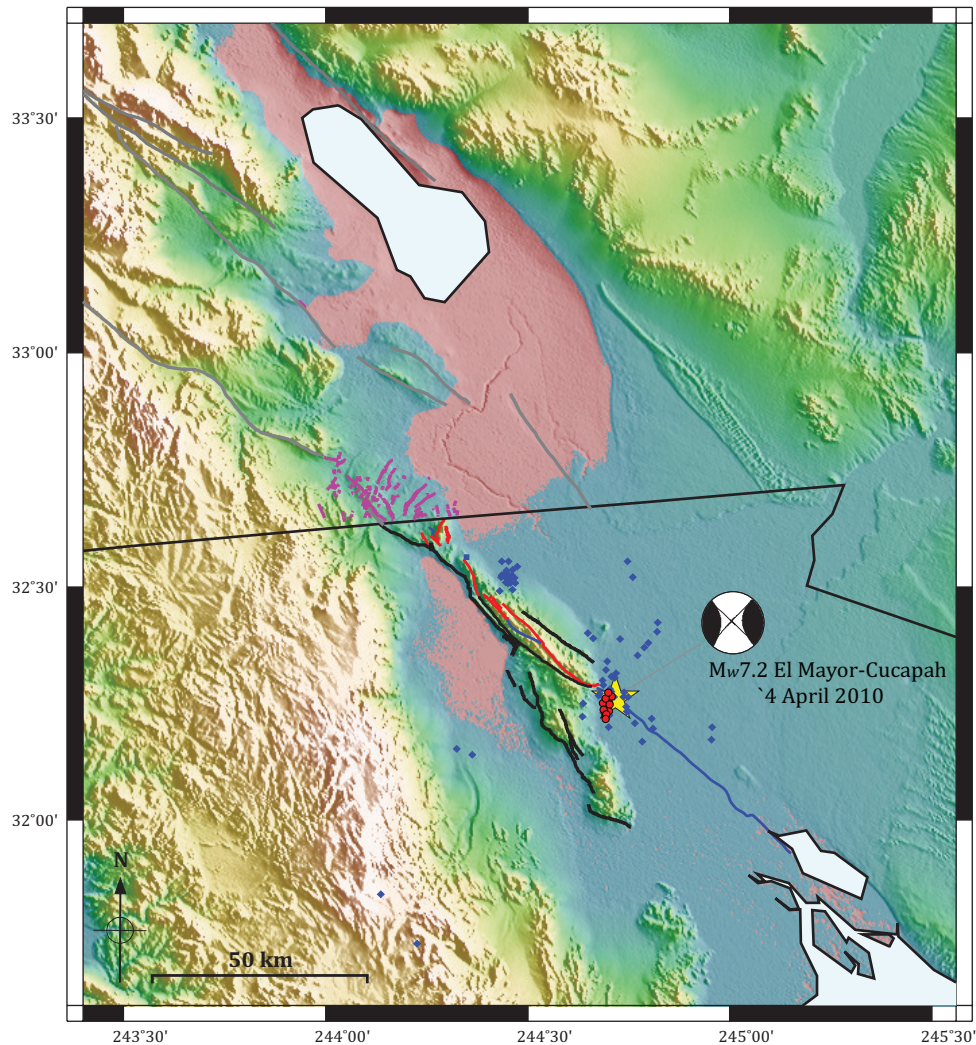


Figure 0.3: Details of the EMC mainshock. Increased seismicity (blue diamonds) was evident in the geothermal and surrounding areas in March 2010. 15 foreshocks (red circles) occurred in the 24 hours preceding the mainshock. The first mainshock subevent occurred at the epicenter (yellow star), and ruptured with normal and dextral motion towards the southeast. A second larger subevent occurred 15 seconds later, and ruptured from the epicenter towards the international border, also with normal and dextral motion [33]. The EMC sequence has a combined moment magnitude of M_w 7.2. This event ruptured ~ 120 km of crust in a complex fashion. Surface rupture, south east of the epicenter (blue line) has been inferred from InSAR data and image cross-correlation [89]. [16] mapped the surface rupture northwest of the epicenter (red lines). Rupture to the northwest occurred in an complicated manner, which included rupture jumping across several fault strands through the Sierra-Cucapah mountain range. Triggered surface slip in the Yuha Desert, mapped by [67] is shown by the pink lines. Additional surface rupture from the 1892 $\sim M7.1$ event was mapped by [17] and is shown by the thick black lines, and southern California faults are shown grey.

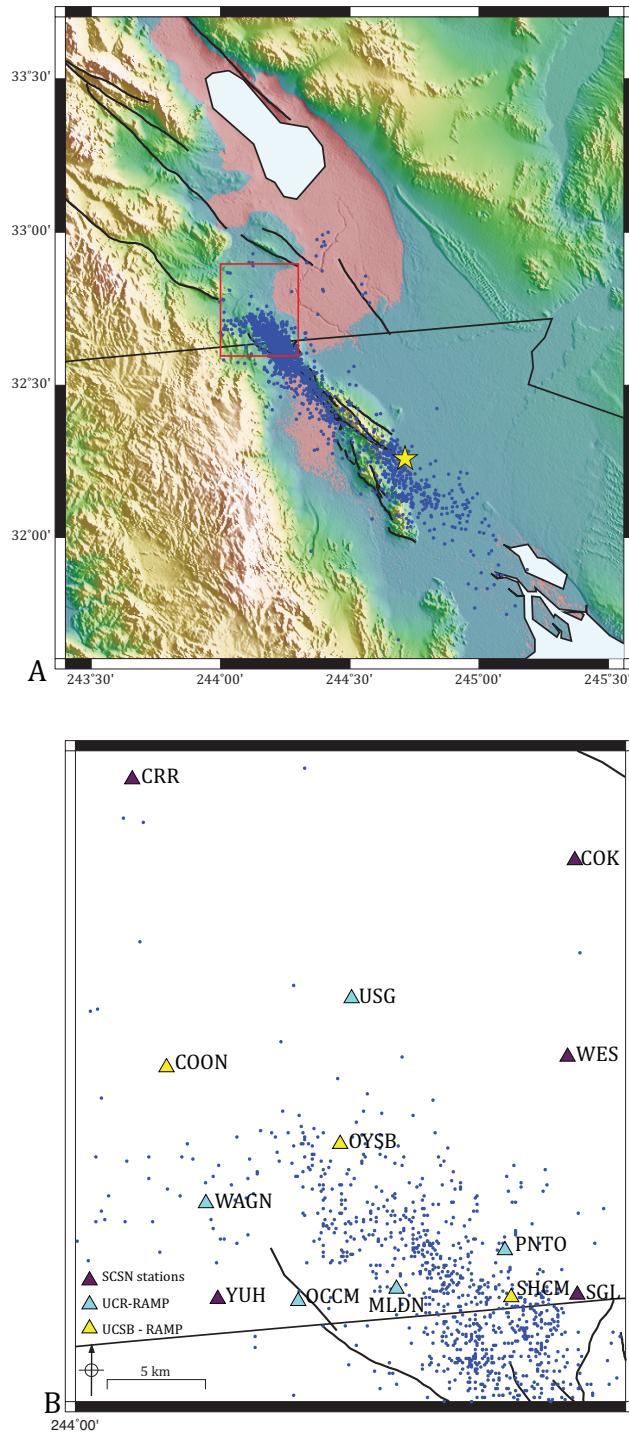
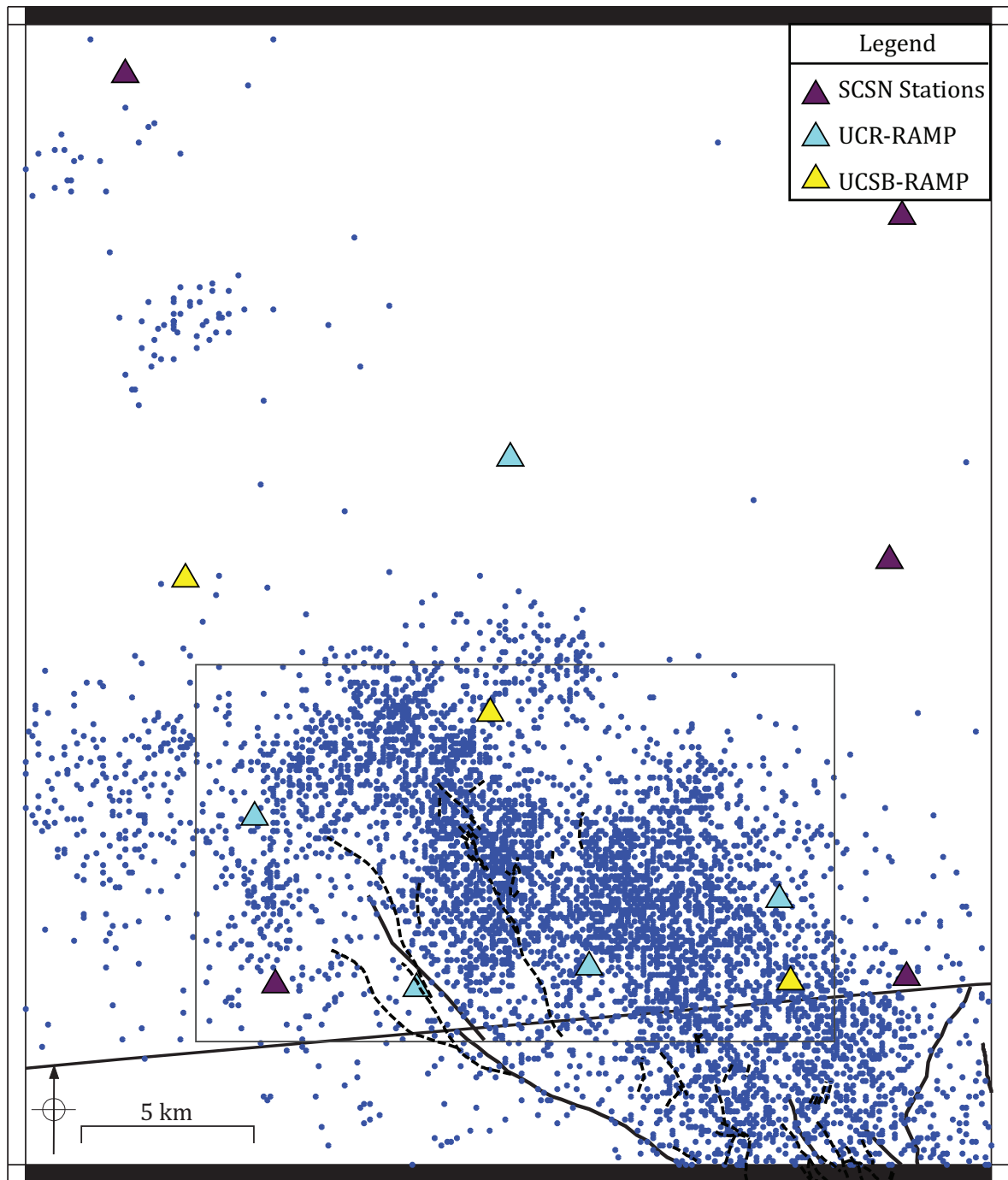


Figure 0.4: A) Aftershocks recorded by the SCSN (blue dots) through of 6 April 2010. Two main aftershock clusters formed within the two days following the mainshock, one in the southeast near the epicenter (yellow star) and the second in the Yuha Desert region, north of the international border. B) An enlarged picture (red box from Figure 4A), showing earthquakes that occurred in the Yuha Desert region following the EMC and before the installation of the UC-RAMP stations (triangles) on 6 April 2010. This area is of particular interest as there are no known through-going fault structures mapped between the Laguna Salada fault in the south and the Elsinore fault in the north.



244°00'

Figure 0.5: An enlarged picture (red box from Figure 4A), showing the events that occurred in the Yuha Desert region during the UC-RAMP deployment period. The study area (outlined by the grey box) contains 4,323 events that are listed in the SCSN catalog. Here, we relocate these events using *hypoDD* [88] and they are used to further assess the fault structure in this area. The relocated seismicity will help determine how strain is accommodated in a region where a through-going plate boundary can not be defined.

Data Processing Flow Chart

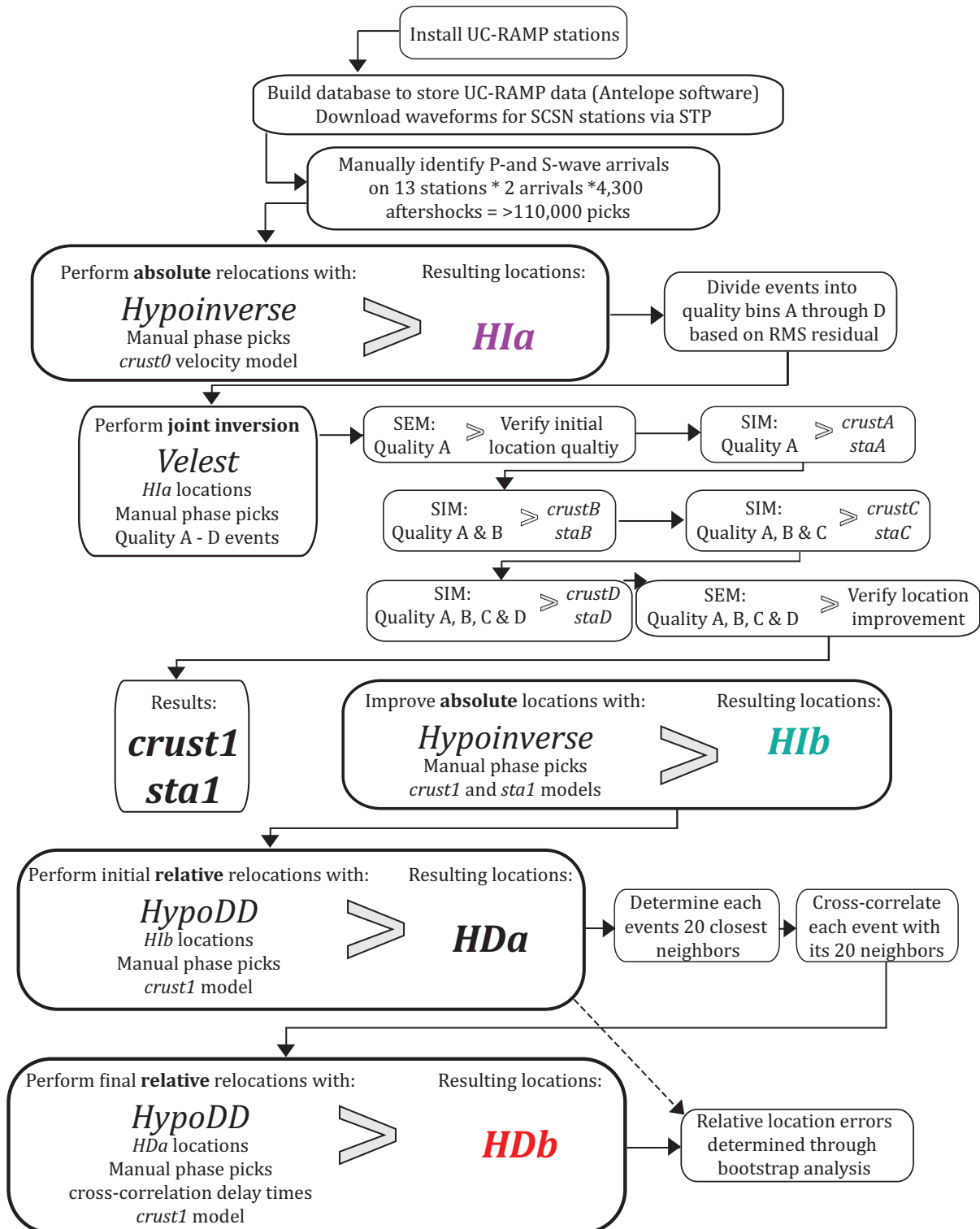


Figure 0.6: Flow chart of the data processing scheme that was used in this analysis. The resulting location codes (i.e. *H1a*, *H1b*, *HDa*, and *HDb*) are color coded according to the color of their corresponding locations as shown in Figure 0.9 (*H1a*), Figure 0.11 (*H1a* and *H1b*), and Figure 0.13 (*H1b* and *HDb*).

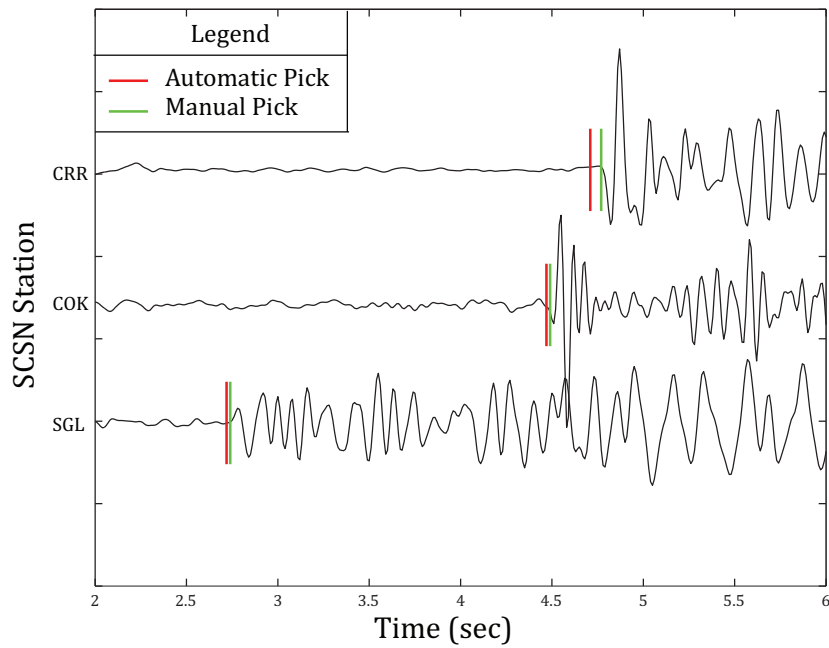
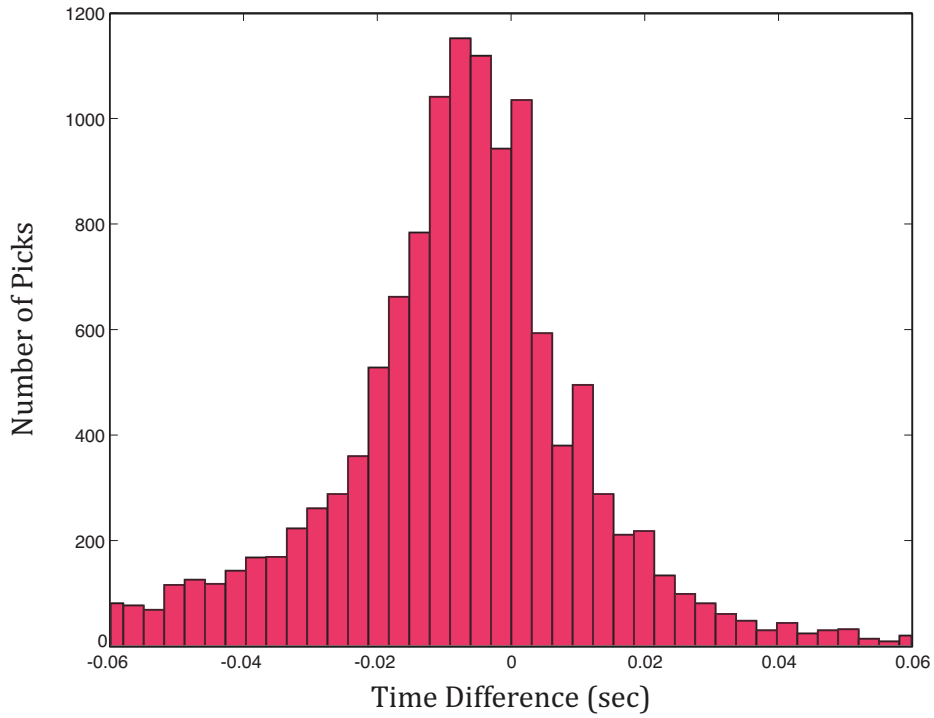


Figure 0.7: Top: Histogram of differences between manual and automatic phase arrival picks. Negative values represent waveforms for which an automatic pick was made before a manual pick. Bottom: Diagram showing the difference in automatic (red line) versus manual (green line) P-wave picks on three of five SCSN stations used in this study. The offset between automatic and manual picks range drastically, between 0 s and 3.0 sec, with a median offset of 0.1289 sec. An arrival misidentified by 0.1 sec can lead to location differences of approximately 1km.

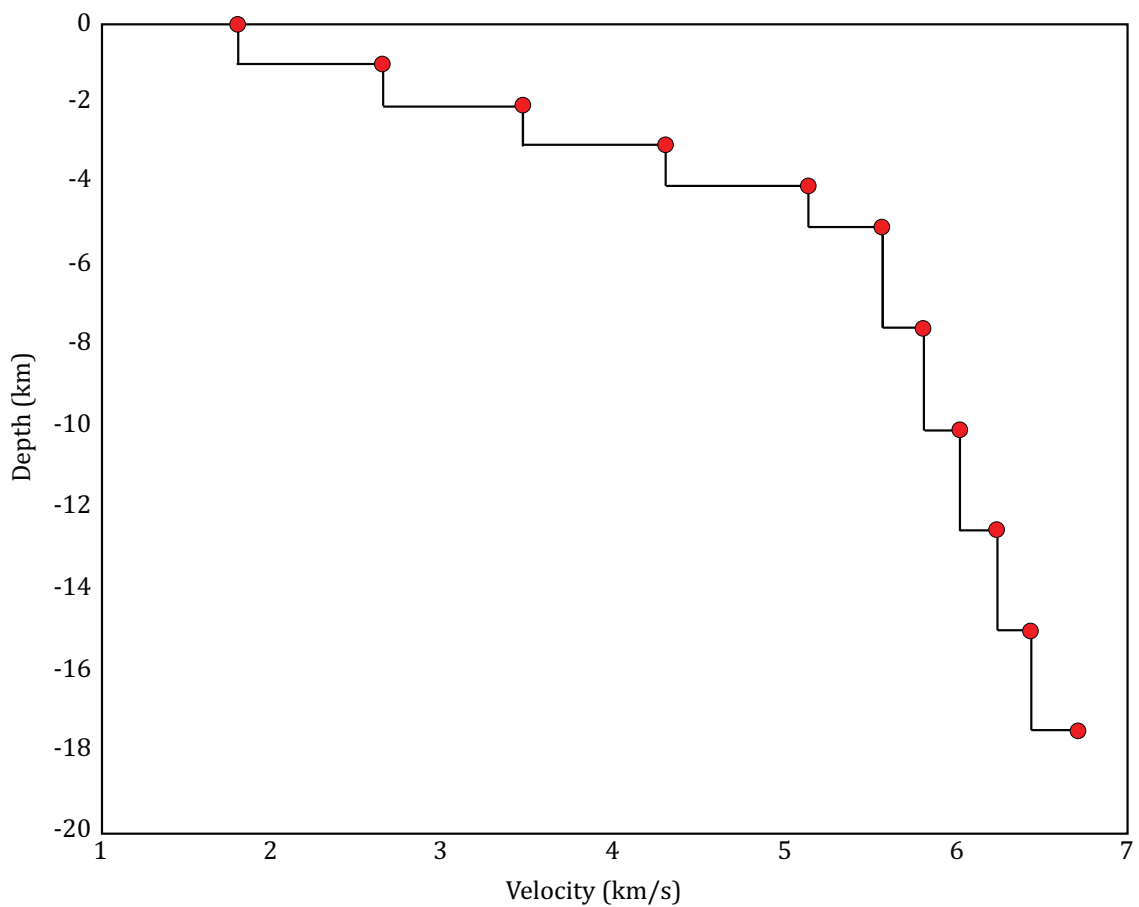


Figure 0.8: *A priori* (*crust0*) velocity model used in the initial absolute location determination with *hypoinverse*. This velocity model was modified from the SCEC Community Velocity Model, version 4 (CVM-v4) for the Imperial Valley region (SCEDC, 2012: <http://www.data.scec.org/research-tools/3d-velocity.html>). We reduced the velocities between the surface and 5 km depth based on a linear interpolation to accommodate the surface sediment layers and reduce the number of air-quakes (e.g. earthquakes that relocate above the Earth's surface) produced through *hypoinverse*.

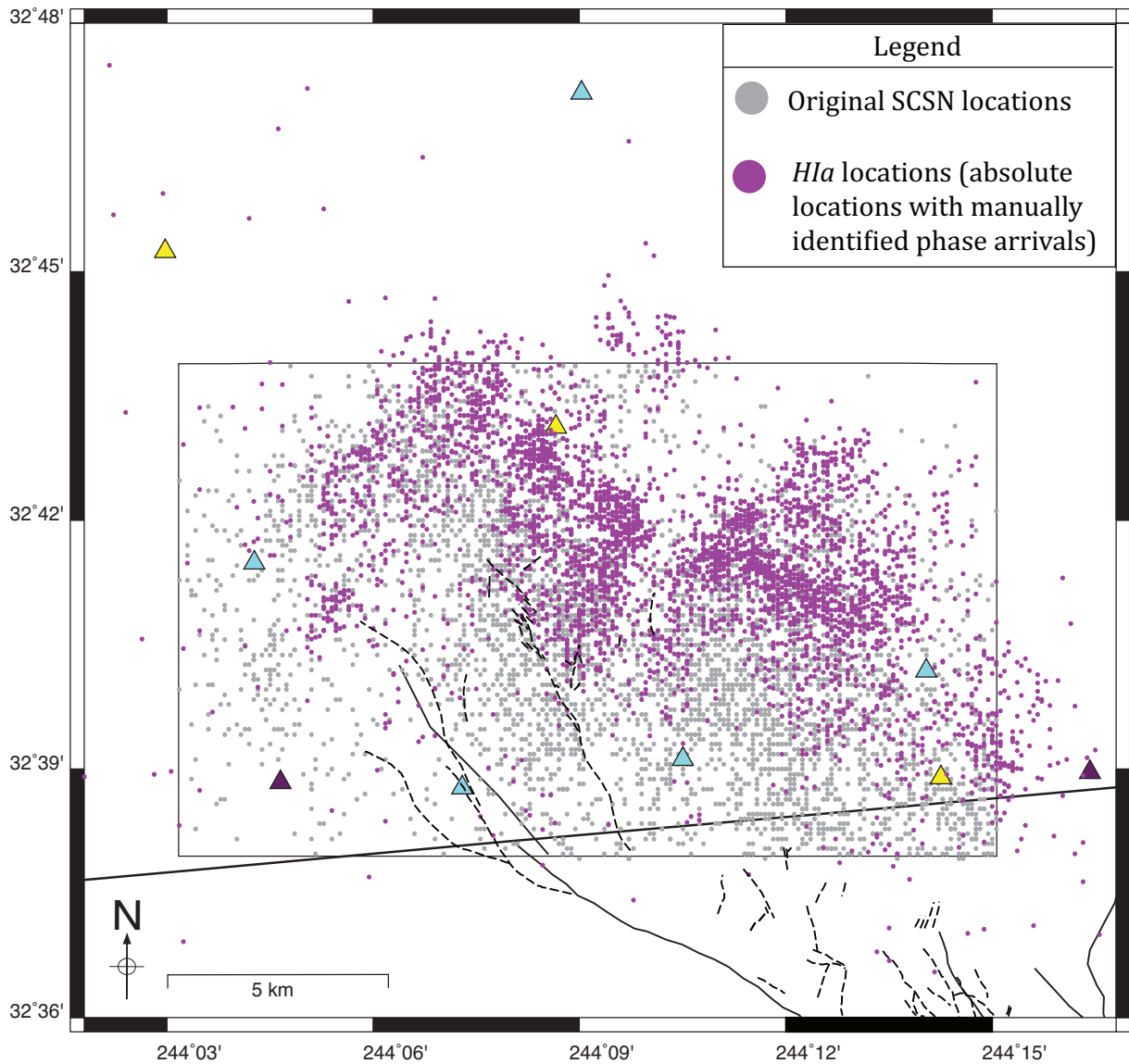


Figure 0.9: Comparison of the first round of relocations with the original SCSN catalog locations. Over 4,300 aftershocks were recorded and located in the Yuba Desert by the SCSN between 6 April and 14 June 2010 (grey dots). P- and S-wave phase arrivals were manually identified for these events and absolute locations were calculated with *hypoinverse* [43] with a modified version of CMV-v4 Imperial Valley input velocity model (*H1a* locations shown by the purple dots) (Figure 0.8). Horizontal and vertical absolute location errors were reduced to 1.5 km and 2.3 km, respectively. RMS timing errors are reduced to 0.25 sec.

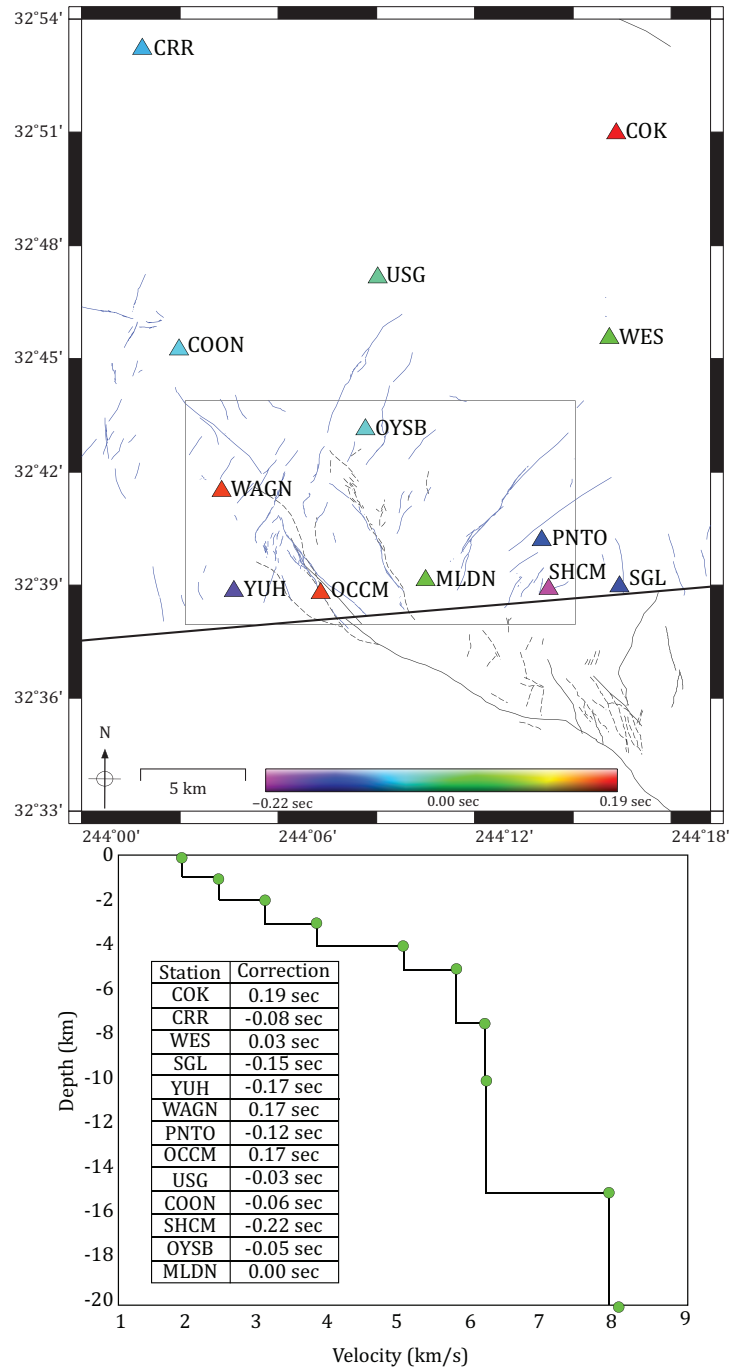


Figure 0.10: Results of the *velest* inversion. Top: The UC-RAMP and 5 SCSN stations used in the inversion are plotted as a function of station correction. The non-uniform distribution of fast and slow station corrections suggest a complicated velocity structure in the Yuba Desert, with many small scale heterogeneities. Faults in green were mapped by [39], faults shown in black were mapped by [17] and those in blue were mapped following the EMC mainshock by [67]. Bottom: The best fitting velocity model (*crust1*) for our station and event distribution that resulted from the *velest* joint inversion. The inversion was completed with the Quality A events from the *HiA* location analysis (see Table 0.1 and Figure 0.9). The inset table lists the associated station corrections.

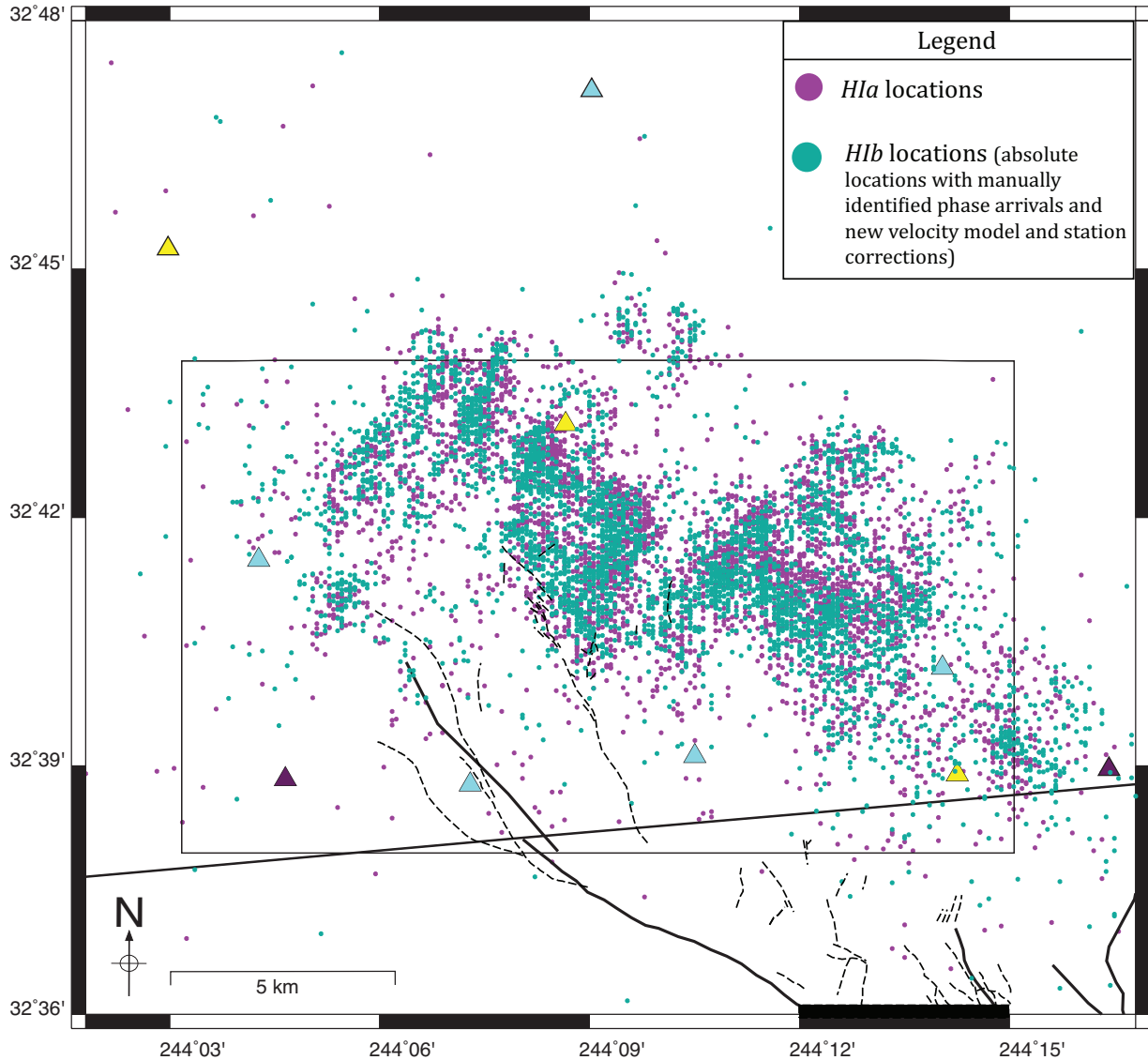


Figure 0.11: Comparison of improved (*H1b*) locations with initial *hypoinverse* locations (*H1a*) (Figure 0.9). The resulting locations (*H1a* locations) from the initial run through *hypoinverse* were separated into quality bins based on RMS residuals (See Table 0.2). The Quality A events were used in a joint inversion analysis to determine station corrections (*sta1*) and a best-fitting velocity model (*crust1*) with the *velast* algorithm. The *sta1* and *crust1* results along with the manual phase picks were incorporated into *hypoinverse*. Horizontal and vertical location errors were reduced to 0.5 km and 1.8 km, respectively. The RMS residual was reduced to 0.13 sec. The *H1b* locations were used as the starting locations in the double-difference relative relocation analysis with *hypoDD* [88].

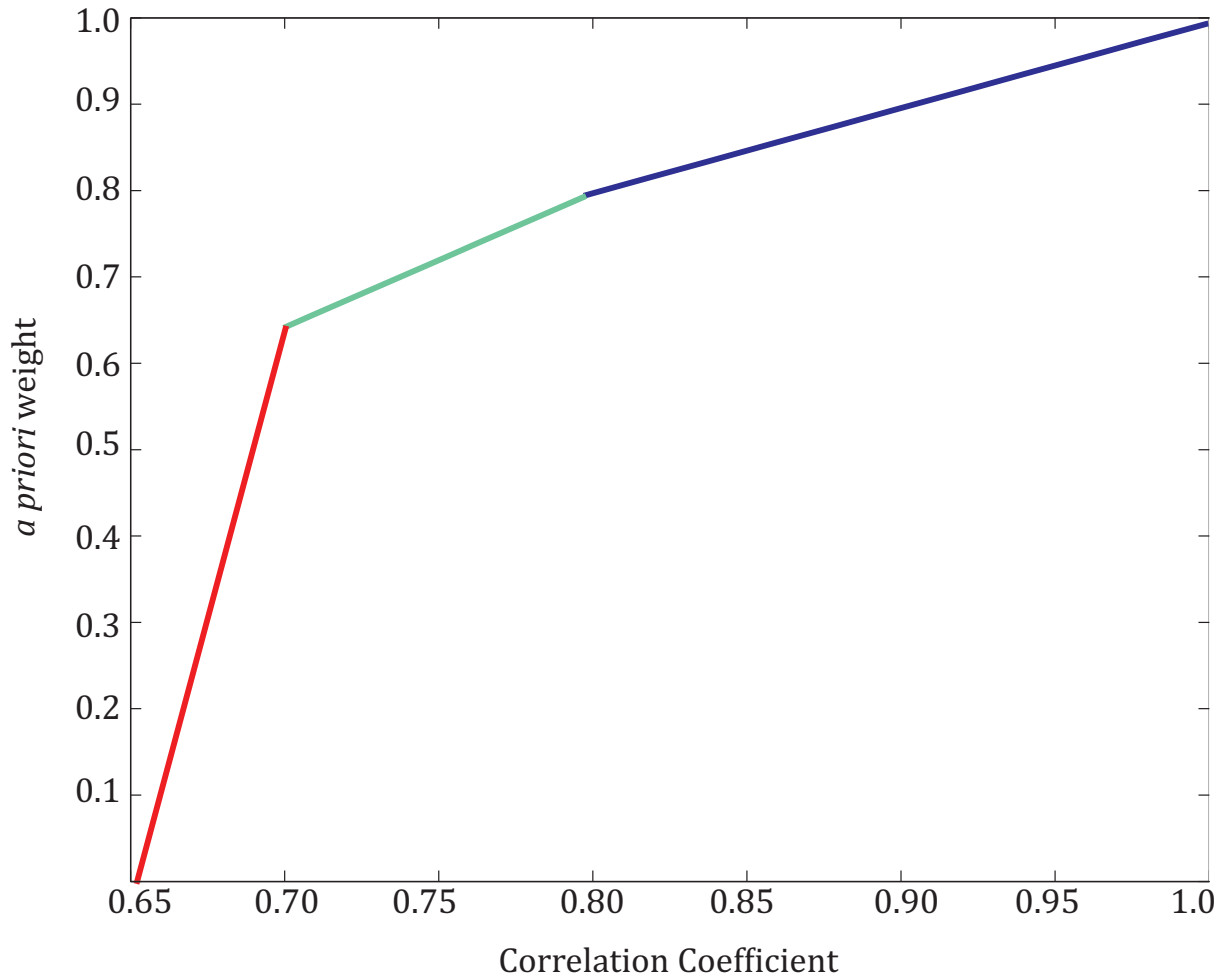


Figure 0.12: Three empirically-derived linear relationships between correlation coefficient and *a priori* weight assignment for P-waves and S-waves. Events with correlation coefficients below 0.7 have been severely down-weighted (red curve), while events with CC values between 0.7 and 0.8 have only been slightly down-weighted (teal curve). Events with the most similarity (i.e. CC greater than 0.8) retain their CC value (blue curve).

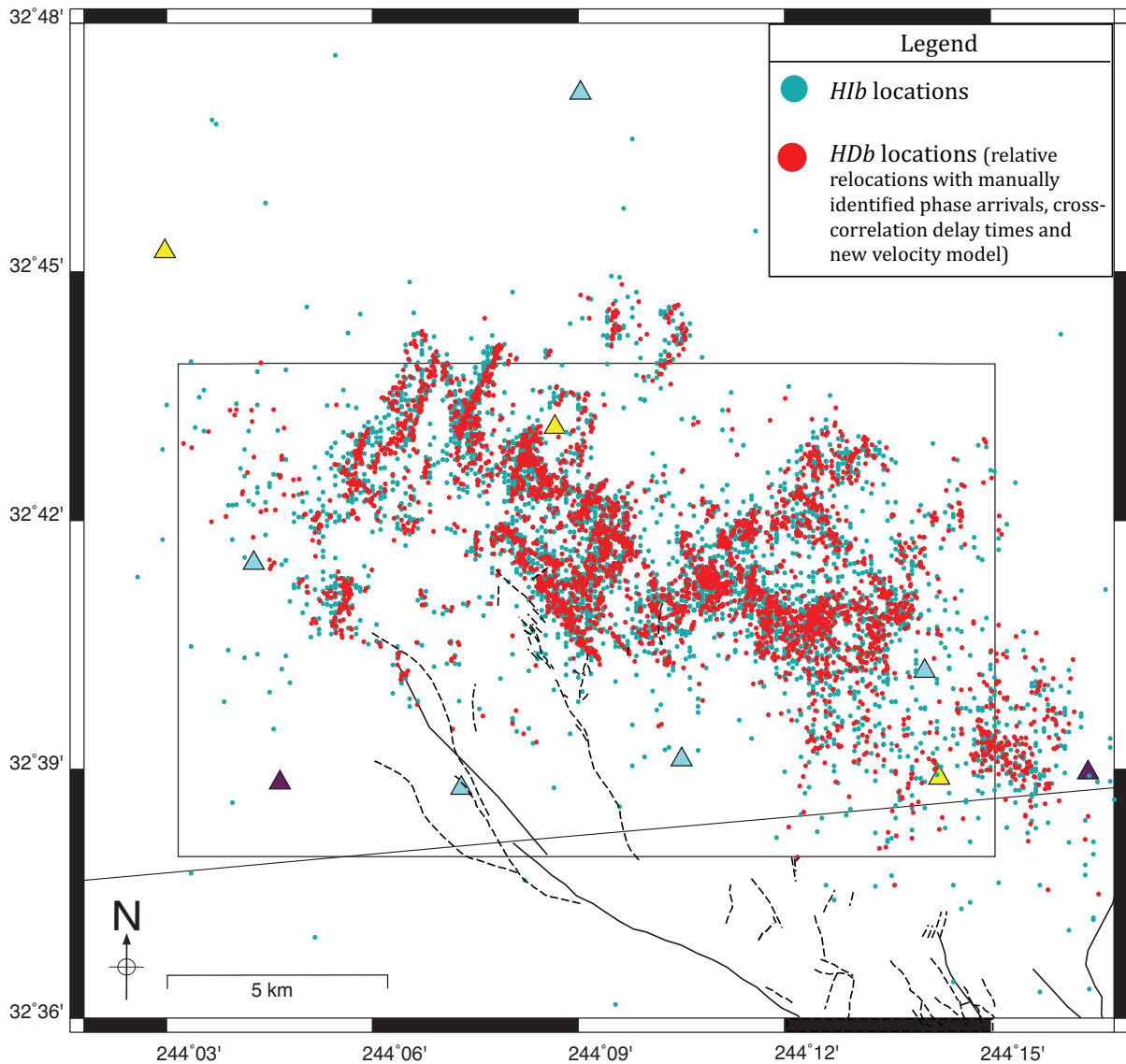


Figure 0.13: Comparison between the absolute locations (*H1b*) and the relative locations (*HDb*). The resulting locations (*HDb* locations) from the double-difference relative relocation are shown in the red dots. The *crust1* velocity model, manual phase arrivals and cross-correlation delay times were used in this analysis. The initial locations used in this step (shown in the teal dots) are the *H1b* absolute locations displayed in Figure 0.11. Relative location errors were estimated to be ~ 20 m horizontally and ~ 80 m vertically through a bootstrap analysis. The RMS timing errors were reduced to 0.004 s.

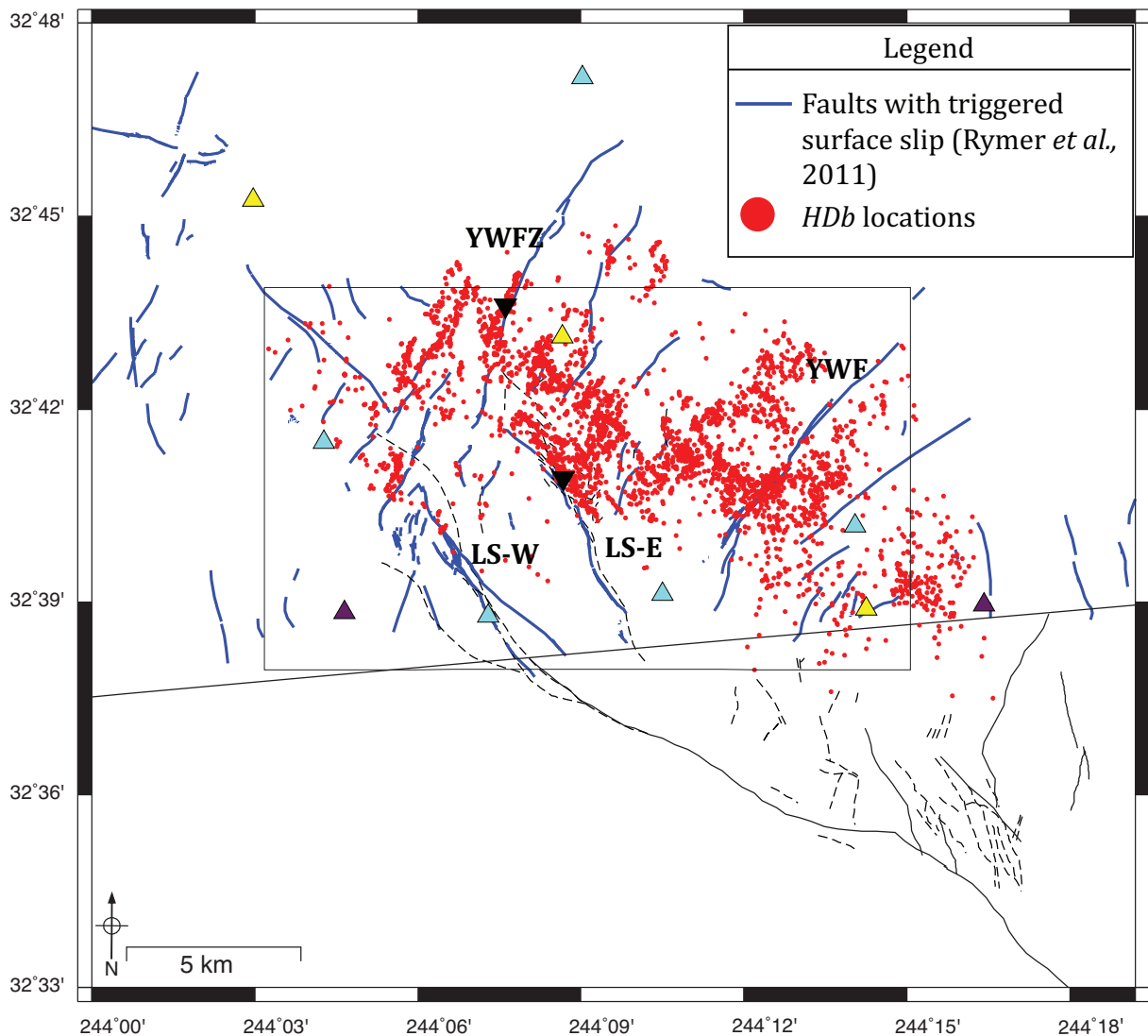


Figure 0.14: The relocated aftershocks that occurred between 6 April and 14 June 2010 are shown by the red dots. Faults mapped in blue were observed to have triggered surface slip following the EMC earthquake [67]. The majority of the seismicity occurred east of the LS-W. The seismicity correlates well with the mapped fault structure of the Yuha Desert. Lineations of seismicity are seen along the right-lateral, northwest trending LS-E branch, along left-lateral northeast trending faults in the Yuha Well Fault Zone, and the Yuha Fault. Inverted black triangles indicate a point along the surface projection of the inferred fault plane shown in cross-section in Figure 0.15.

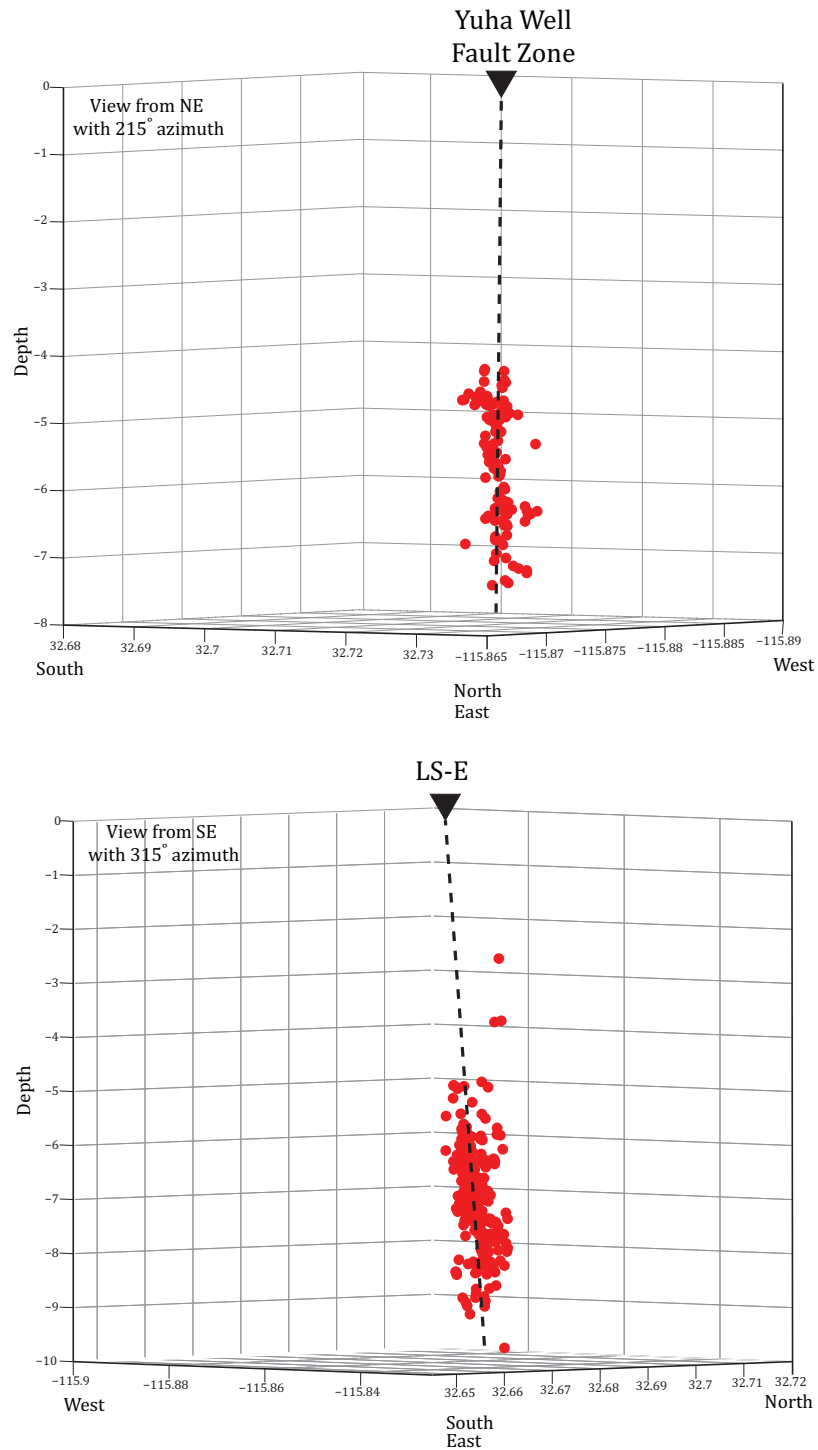


Figure 0.15: Three-dimensional cross-sectional views where seismicity is highly correlated with mapped faults showing triggered surface slip. Left: A prominent fault of the Yuha Well Fault Zone is correlated with relocated seismicity (red dots) that forms a nearly vertical plane (heavy dashed line). The inferred plane dips $\sim 89^\circ$ SE and projects to the surface (shown by inverted black triangles in Figure 0.14 at the approximately location of the fault mapped by [67]). Right: Seismicity highlighting the LS-E (red dots) correlates well with the projection of the fault to the surface (heavy dashed line). The inferred subsurface extension of the LS-E dips $\sim 85^\circ$ NE.

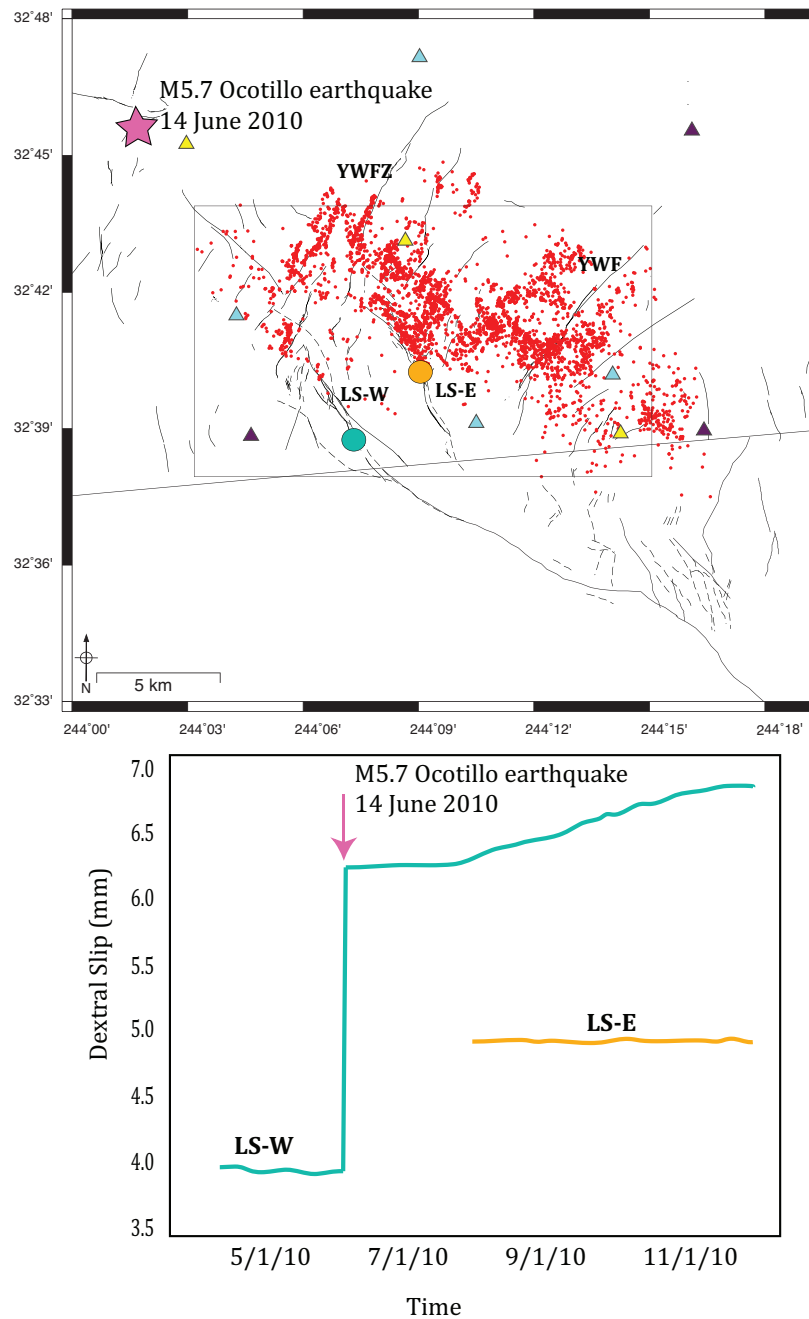


Figure 0.16: Comparison between the mapped triggered surface slip [67], relocated seismicity and data collected from two creepmeters installed along the LS-W and LS-E. Top: Red dots indicate the relocated seismicity, plotted along with the fault structure in the Yuha Desert area. The green and yellow circles along the LS-W and LS-E branches, respectively, represent the two creepmeters installed in the area. The LS-W creepmeter was installed 10 April 2010, while the LS-E creepmeter was not installed until 14 August 2010. Bottom: Creepmeter time series (data courtesy of Roger Bilham, 2012) show ~ 2 mm of surface creep on the LS-W occurring coincident with the M5.7 Ocotillo earthquake. While the LS-E creepmeter was not installed during this event, surface displacement was not observed in the precise caliper measurements taken along this fault segment.

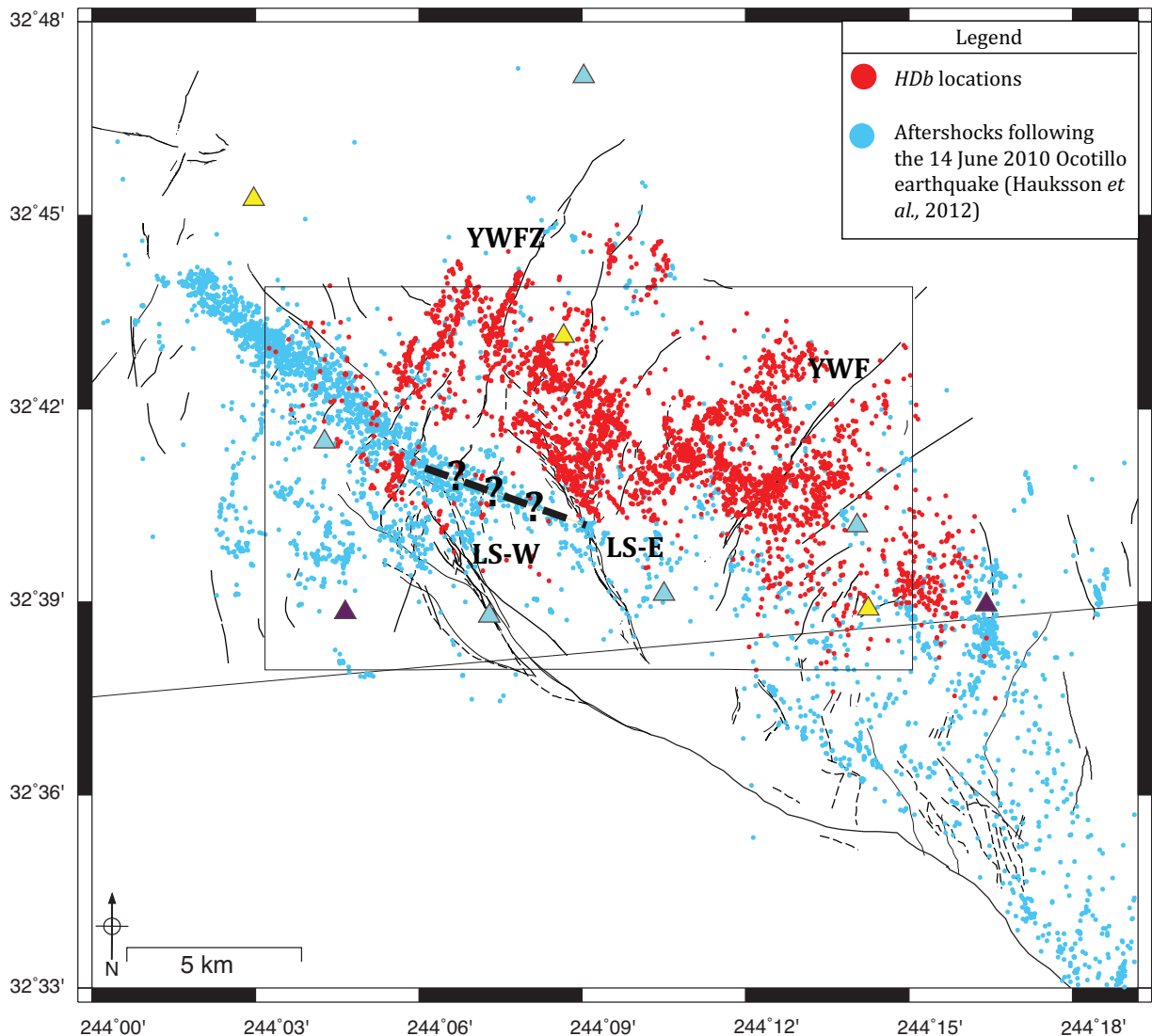


Figure 0.17: Comparison of aftershocks that occurred in response to the EMC mainshock (red dots) and the Ocotillo earthquake (blue dots). The aftershocks plotted in red occurred between 6 April and 14 June 2010, the two month period between the EMC and Ocotillo events. The locations shown in red are relocated in this work. The aftershocks plotted in blue were relocated by [31], and occurred after the Ocotillo earthquake. This temporal plot shows that the LS-E is seismicity active before the Ocotillo event, however it shuts down and seismicity transfers to the LS-W. Surface creep was not seen on the LS-E following either earthquake; however, the LS-W was observed to creep ~ 2 mm in response to the Ocotillo earthquake. Additionally, the seismicity that occurred following the Ocotillo earthquake appears to form a connection between the LS-W and LS-E on an unmapped fault segment (indicated by the arrow and highlighted by the orange dashed line).

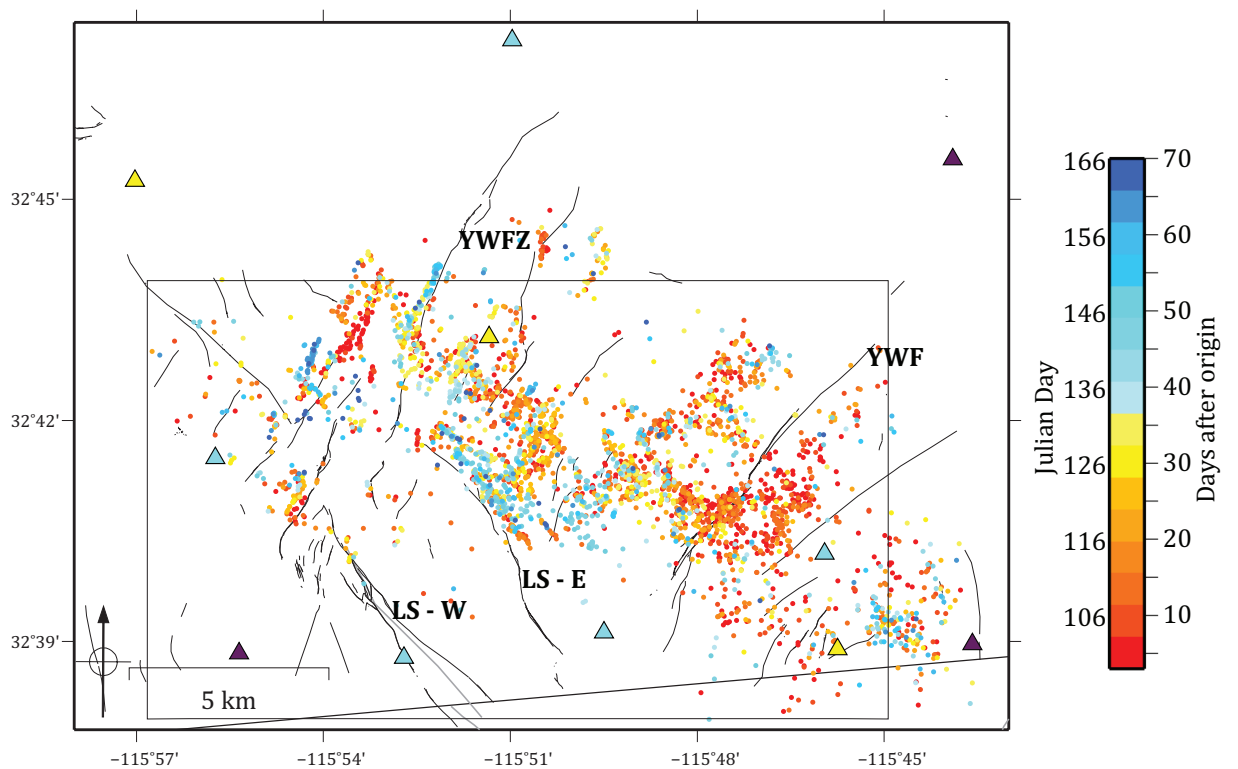


Figure 0.18: Relocated seismicity plotted as a function of time after the EMC mainshock. A non-uniform expansion of aftershock activity is seen following the mainshock. Some areas are active early, namely the south of the Yuha Well fault and one of the en echelon northeast trending segments of Yuha Well Fault Zone. Additional early activity forms a northwest trending band adjacent to the LS-E. Activity in the areas that show seismic deformation shortly after the EMC mainshock, become relatively inactive, or shut off completely. After ~ 40 days, the majority of deformation is accommodated along the LS-E and in the Yuha Well Fault Zone.

Bibliography

- [1] Michael Antolik, R. E. Abercrombie, and G. Ekström. The 14 November 2001 Kokoxili (Kunlunshan), Tibet, earthquake: Rupture transfer through large extensional step-over. *Bull. Seism. Soc. Am*, 94:1173–1194, 2004.
- [2] Y. Ben-Zion. Stress, slip, and earthquakes in models of complex single-fault systems incorporating brittle and creep deformations. *Journal of Geophys. Res.*, 101:5677–5706, 1996.
- [3] Roger Bilham. SURFACE SLIP SUBSEQUENT TO THE 24 NOVEMBER 1987 SUPERSITION HILLS, CALIFORNIA, EARTHQUAKE MONITORED BY DIGITAL CREEPMETERS. *Bull. Seism. Soc. Am*, 79:424–450, 1989.
- [4] P Bormann. *New Manual of Seismological Observatory Practice (NMSOP-2)*,. IASPEI, 2012.
- [5] E Bozkurt and Koçyiôit. The Kazova basin: an active negative flower structure on the Almus Fault Zone, a splay fault of the system of the North Anatolian Fault Zone, Turkey. *Tectonophysics*, 256:239–254, 1996.
- [6] C Chairabba and A Frepoli. Minimum 1D velocity models in central and southern Italy: a contribution to better constrain hypocentral determinations. *Annals of Geophysics*, 40, 1997.

- [7] Chung-Han Chan and Ross S Stein. Stress evolution following the 1999 Chi-Chi, Taiwan, earthquake: consequences for afterslip, relaxation, aftershocks and departures from Omori decay. *Geophys. J. Int.*, 177:179–192, 2009.
- [8] J C Crowell. What we know and do not know about the history of the San Andreas fault. Conference on Earth and Space Science: University of California, Los Angeles, 1978.
- [9] Shamita Das and Christopher H Scholz. Off-fault aftershock clusters caused by shear stress increase? *Bull. Seism. Soc. Am.*, 71:1669–1675, 1981.
- [10] T W Jr. Dibblee. *Geology of the Imperial Valley region, California*, volume 170. Bull. California Div. Mines and geol., 1954.
- [11] J. H. Dieterich. A constitutive law for rate of earthquake production and its application to earthquake clustering. *Journal of Geophys. Res.*, 99:2601–2618, 1994.
- [12] Roy K Dokka and Richard H Merriam. Late Cenozoic extension of northeastern Baja California, Mexico. *Geol. Soc. Amer. Bull.*, 93:371–388, 1982.
- [13] Tim P Dooley and Ken R McClay. Strike-slip deformation in the Confidence Hills, southern Death Valley fault zone, eastern California, USA. *Journal of the Geological Society*, 153:375–387, 1996.
- [14] Wen-Xuan Du, Clifford H Thurber, and Donna Eberhart-Phillips. Earthquake relocation using cross-correlation time delay estimates verified with the bispectrum method. *Bull. Seism. Soc. Am.*, 94(3):856–866, 2004.
- [15] Benchun Duan and David D Oglesby. Heterogeneous fault stresses from previous earthquakes and the effect of dynamics of parallel strike-slip faults. *Journal of Geophys. Res.*, 111:B05309, 2006.

- [16] J M Fletcher, T K Rockwell, Orlando Teran, Masana E, G Faneros, K W Hudnut, J Gonzales, A Gonzalez, R Spelz, and K J Mueller. The surface ruptures associated with the El Mayor-Borrego earthquake sequence. *Geological Society of America Abstracts*, 2010.
- [17] John M Fletcher and Ronald M Spelz. Patterns of Quaternary deformation and rupture propagation associated with an active low-angle normal fault, Laguna Salada, Mexico: Evidence of a rolling hinge? *Geosphere*, 5:385–407, 2009.
- [18] A M Frassetto, George Zandt, Hersh Gilbert, Thomas L Owens, and Craig H Jones. Structure of the Sierra Nevada from receiver functions and implications for lithospheric foundering. *Geosphere*, 7:898–921, 2011.
- [19] Andrew M Freed. Earthquake triggering by static, dynamic, and postseismic stress transfer. *Annu. Rev. Earth Planet. Sci.*, 33:335–367, 2005.
- [20] Gary S Fuis and William M Kohler. Crustal structure and tectonics of the Imperial Valley region, California. In Catherine A. Rigsby, editor, *The Imperial Basin - Tectonics, Sedimentaries, and Thermal Aspects: Pacific Section S.E.P.M.*, pages 1–13, 1984.
- [21] J L Got, J Fréchet, and Fred W Klein. Deep fault plane geometry inferred from multiplet relative relocation beneath the south flank of Kilauea. *J. of Geophys Res.*, 99(B8):15375–15386, 1994.
- [22] N R Goultry, R O Burford, C R Allen, R Gilman, C E Johnson, and R P Keller. LARGE CREEP EVENTS ON THE IMPERIAL FAULT, CALIFORNIA. *Bull. Seism. Soc. Am.*, 68:517–521, 1978.

- [23] D M Hadley and H. Kanamori. Seismic structure of the Transverse Ranges, California. *Geol. Soc. Amer. Bull.*, 88:1461–1478, 1977.
- [24] T P Harding. Newport-Inglewood Trend, California - An Example of Wrench Style of Deformation. *Amer. Assoc. Petro. Geol. Bull.*, 57:97–116, 1973.
- [25] T P Harding. Seismic Characteristics and Identification of Negative Flower Structures, Positive Flower Structures, and Positive Structural Inversion. *Amer. Assoc. Petro. Geol. Bull.*, 69:582–600, 1985.
- [26] T P Harding. Interpretation of Footwall (Lowside) Fault Traps Sealed by Reverse Faults and Convergent Wrench Faults. *Amer. Assoc. Petro. Geol. Bull.*, 72:738–757, 1988.
- [27] T P Harding. Identification of Wrench Faults Using Subsurface Structural Data: Criteria and Pitfalls. *Amer. Assoc. Petro. Geol. Bull.*, 74:1590–1609, 1990.
- [28] R A Harris and S M Day. Dynamic 3D simulations of earthquakes on en echelon faults. *Geophys. Res. Lett.*, 26:2089–2092, 1999.
- [29] Ruth A Harris and Steven M Day. Dynamics of fault interaction: Parallel strike-slip faults. *Journal of Geophys. Res.*, 98:4461–4472, 1993.
- [30] E Hauksson, Lucile M Jones, and K. Hutton. The 1999 M_w 7.1 Hector Mine, California, earthquake sequence: Complex conjugate strike-slip faulting. *Bull. Seism. Soc. Am.*, 92:Hauksson, E and Jones, Lucile M and Hutton, K., 2002.
- [31] E Hauksson, W. Yang, and P M Shearer. Waveform relocated earthquake catalog for southern California (1981 to 2011). *Bull. Seism. Soc. Am.*, 2012.
- [32] Egill Hauksson and Peter Shearer. Southern California hypocenter relocation with

- waveform cross- correlation, part 1: Results using the double-difference method. *Bull. Seism. Soc. Am*, 3(3):896–903, 2005.
- [33] Egill Hauksson, Joann Stock, Kate Hutton, Wenheng Yank, J Antonio Vidal-Villegas, and Hiroo Kanamori. The 2010 M_w 7.2 El Mayor-Cucapah earthquake sequence, Baja California, Mexico and southernmost California, USA: Active seismotectonics along the Mexican Pacific margin. *Pure Appl. Geophys*, 2010.
- [34] A Helmstetter, Guy Ouillon, and Didier Sornette. Are aftershocks of large Californian earthquakes diffusing? *GEOP*, 2003.
- [35] D P Hill, P. A. Reasenberg, A Michael, W J Arabaz, G C Beroza, D Brumbaugh, J N Brune, R. Castro, S Davis, D dePolo, W Ellsworth, J. Gomberg, S Harmsen, L House, S M Jackson, M J S Johnston, L Jones, R Keller, S Malone, L Munguia, S Nava, J. C. Pechmann, A Sanford, R W Simpson, R B Smith, M Stark, M Stickney, A Vidal, S Walter, V. M. Wong, and J Zollweg. Seismicity remotely triggered by the magnitude 7.3 Landers, California, earthquake. *Science*, 260:1617–1623, 1993.
- [36] Ya-Hu Hsu, Jean-Philippe Simons, Mark ad Avouac, John Galetzka, Kerry E Sieh, Mohamed Chlieh, Danny Natawidjaja, Linette Prawirodirdjo, and Yeduha Bock. Frictional afterslip following the 2005 Nias-Simeulue earthquake, Sumatra. *Science*, 312, 2006.
- [37] K W Hudnut and K E Sieh. BEHAVIOR OF THE SUPERSITION HILLS FAULT DURING THE PAST 330 YEARS. *Bull. Seism. Soc. Am*, 79:304–329, 1989.
- [38] K. Hutton, E Hauksson, John Clinton, Joseph Franck, Anthony Guarino, Nick

- Scheckel, Doug Given, and Alan Yong. Southern California Seismic Network update. *SRL*, 77, 2006.
- [39] Sharon Isaac. Geology and structure of the Yuha Desert between Ocotillo, California, U.S.A, and Laguna Salada, Baja California, Mexico. Masters thesis, San Diego State University, 1987.
- [40] Jordi Juliá, Andrew A Nyblade, Ray Durrheim, Lindsay Linzer, Rengin Gök, Paul Dirks, and William Walter. Source Mechanisms of Mine-Related Seismicity, Savuka Mine, South Africa. *Bull. Seism. Soc. Am*, 99:2801–2814, 2009.
- [41] Geoffrey C P King, Ross S Stein, and Jian Lin. Static Stress Changes and the Triggering of Earthquakes. *Bull. Seism. Soc. Am*, 84:935–953, 1994.
- [42] E Kissling, W Ellsworth, D. Eberhart-Phillips, and U Kradolfer. Initial reference models in local earthquake tomography. *Journal of Geophys. Res.*, 99:19,635–19,646, 1994.
- [43] F W Klein. *User’s Guide to HYPOINVERSE-2000, a Fortran Program to Solve for Earthquake Locations and Magnitudes*. USGS, 2002.
- [44] Julian C Lozos, D. D. Oglesby, B. Duan, and Steven G Wesnousky. The effects of double fault bends on rupture propagation: A geometrical parameter study. *Bull. Seism. Soc. Am*, 101:385–398, 2011.
- [45] Suzanne N Lyons, Yehuda Bock, and David T Sandwell. Creep along the Imperial Fault, southern California, from GPS measurements. *Journal of Geophys. Res.*, 107:2249, 2002.
- [46] Kuo-Fong Ma and Chung-Han Chan. Response of seismicity to Coulomb stress

- triggers and shadows of the 1999 $M_w = 7.6$ Chi-Chi, Taiwan, earthquake. *Journal of Geophys. Res.*, 110:B05S19, 2005.
- [47] Laurent Maerten. Variation in slip on intersecting normal faults: Implications for paleostress inversion. *Journal of Geophys. Res.*, 2000.
- [48] Harold Magistrale and Thomas Rockwell. The central and southern Elsinore fault zone, southern California. *Bull. Seism. Soc. Am.*, 6(6):1793–1803, 1996.
- [49] Sally F McGill, Clarence R Allen, Kenneth W Hudnut, David C Johnson, Wayne F Miller, and Kerry E Sieh. SLIP ON THE SUPERSITION HILLS FAULT AND ON NEARBY FAULTS ASSOCIATED WITH THE 24 NOVEMBER 1987 ELMORE RANCH AND SUPERSITION HILLS EARTHQUAKES, SOUTHERN CALIFORNIA. *Bull. Seism. Soc. Am.*, 79:362–375, 1989.
- [50] Carlos Mendoza and Stephen H Hartzell. AFTERSHOCK PATTERNS AND MAIN SHOCK FAULTING. *Bull. Seism. Soc. Am.*, 78:1438–1449, 1988.
- [51] K J Mueller. Neotectonics, alluvial history and soil chronology of the southwestern margin of the Sierra de Los Cucapas, Baja California Norte. Master’s thesis, San Diego State University, 1984.
- [52] Karl J Mueller and Thomas K Rockwell. Late Quaternary activity of the Laguna Salada fault in northern Baja California, Mexico. *GSA Bulletin*, 107(1):8–18, 1995.
- [53] J Noir, S Békri, P M Adler, P Tapponnier, and G C P King. Fluid flow triggered migration of events in the 1989 Dobi earthquake sequence of central Afar. *Geophys. Res. Lett.*, 24:2335–2338, 1997.
- [54] Anibal Ojeda and Jens Havskov. Crustal structure and local seismicity in Colombia. *Journal of Seismology*, 5:575–593, 2001.

- [55] F Omori. On the after-shocks of earthquakes. *J. Coll. Sci. Tokio Imp. Univ.*, 136:111–2000, 1894.
- [56] Z. Peng and Peng Zhao. Migration of early aftershocks following the 2004 Parkfield earthquake. *Nat. Geosci.*, 2, 2009.
- [57] H Perfettini and Jean-Philippe Avouac. Postseismic relaxation driven by brittle creep: A possible mechanism to reconcile geodetic measurements and the decay rate of aftershocks, application to the Chi-Chi earthquake, Taiwan. *Journal of Geophys. Res.*, 109:B02304, 2004.
- [58] C T Pinault and T K Rockwell. Rates and sense of Holocene faulting on the southern Elsinore fault; further constraints on the distribution of dextral shear between the Pacific and North American plates. *Geological Society of America Abstracts with Programs*, 16:624, 1984.
- [59] B Pontoise and T Monfret. Shallow seismogenic zone detected from an offshore-onshore temporary seismic network in the Esmeraldas area (northern Ecuador). *Gcubed*, 5, 2004.
- [60] G Poupinet, W Ellsworth, and J Frechet. Monitoring velocity variations in the crust using earthquake doublets: An application to the Calaveras Fault, California. *J. of Geophys Res.*, 89(B7):5719–5731, 1984.
- [61] N A Ratchkovski, R A Hansen, J C Stachnik, T Cox, O Fox, L Rao, E Clark, M Lafevers, S Estes, J B MacCormack, and T Williams. Aftershock sequence of the M_w 7.9 Denali fault, Alaska, earthquake of 3 November from regional seismic network data. *SRL*, 2003.
- [62] P. A. Reasenbergs and W Ellsworth. Aftershocks of the Coyots Lake, California,

- earthquake of August 6,1979; a detailed study. *Journal of Geophys. Res.*, 87:10,637–10,655, 1982.
- [63] Keith B Richards-Dinger and Peter M Shearer. Earthquake locations in southern California obtained using source-specific station terms. *J. of Geophys Res.*, 105(B5):10939–10960, 2000.
- [64] D P Robinson, C Brough, and S Das. The W_w 7.8, 2001 Kunlunshan earthquake: Extreme rupture speed variability and effect of fault geometry. *Journal of Geophys. Res.*, 11:B08303, 2006.
- [65] A M Rubin, D Gillard, and J L Got. Streaks of microearthquakes along creeping faults. *Nature*, 400:635–641, 1999.
- [66] Kacper Rybicki. Analysis of aftershocks on the basis of dislocation theory. *Phys. Earth. Planet. Inter.*, 7:409–422, 1973.
- [67] M J Rymer, Jerome A Treiman, Katherine J Kendrick, James J Linenkaemper, Ray J Weldon, R Bilham, Meng Wei, E Fielding, Janis L Hernandez, Brian P E Olson, Pamela J Irvine, Nichole Knepprath, Robert R Sickler, Xiaopeng Tong, and Martin E Siem. Triggered surface slips in southern California associated with the 2010 El Mayor-Cucapah, Baja California, Mexico, earthquake, USGS Open-File Report 2010-1333. Technical report, 2011.
- [68] D P Schaff, G H R Bokelmann, G C Beroza, F Waldhauser, and W L Ellsworth. High resolution image of Calaveras Fault seismicity. *J. Geophys Res.*, 107:2186, 2002.
- [69] David P Schaff, G:otz H R Bokelmann, William L Ellsworth, Eva Zanzerkia, Felix

- Walhauser, and Gregory C Beroza. Optimizing correlation techniques for improved earthquake location. *Bull. Seism. Soc. Am*, 94(2):705–721, 2004.
- [70] David P Schaff and Felix Waldhauser. Waveform cross-correlation-based differential travel-time measurements at the northern california seismic network. *Bull. Seism. Soc. Am*, 95(6):2446–2461, 2005.
- [71] P Segall and D D Pollard. Mechanics of discontinuous faults. *Journal of Geophys. Res.*, 85:4337–4350, 1980.
- [72] Robert V Sharp. San Jacinto Fault Zone in teh Peninsular Ranges of southern California. *Geol. Soc. Amer. Bull.*, 78:705–730, 1967.
- [73] Peter M Shearer. Improving local earthquake locations using the L1 norm and waveform cross correlation: Application to the Whittier Narrows, California, aftershock sequence. *J. of Geophys Res.*, 102(B4):8269–8283, 1997.
- [74] Peter M Shearer, Egill Hauksson, and Guoqing Lin. Southern California hypocenter relocation with waveform cross-correlation, part 2: Results using source-specific station terms and cluster analysis. *Bull. Seism. Soc. Am*, 95(3):904–915, 2005.
- [75] R W Simpson, M Barall, J Langbein, J R Murray, and M J Rymer. San Andreas Fault geometry in the Parkfield, California, region. *Bull. Seism. Soc. Am*, 96:S28–S37, 2006.
- [76] A T Smith and P Kasameyer. Microseismicity study of the El Hoyo-Monte Galan Geothermal Prospect, Nicaragua. Lawrence Livermore National Laboratory, Livermore, California, 1997.
- [77] R. S. Stein and Michael Lisowski. The 1979 Homestead Valley earthquake sequence,

- California: Control of aftershocks and postseismic deformations. *Journal of Geophys. Res.*, 88:6477–6490, 1983.
- [78] Danielle F Sumy, J B Gaherty, W-Y Kim, T Diehl, and J Collins. The mechanics of earthquakes and faulting in the Gulf of California. *Bull. Seism. Soc. Am.* (*inpress*), 2012.
- [79] Fumiko Tajima and H. Kanamori. Global survey of aftershock area expansion patterns. *Phys. Earth. Planet. Inter.*, 40:77–134, 1985.
- [80] Hong Kie Thio and H. Kanamori. Source complexity of the 1994 Northridge earthquake and its relation to aftershock mechanisms. *Bull. Seism. Soc. Am.*, 86:S84–S92, 1996.
- [81] Shinji Toda and Shozo Matsumura. Spatio-temporal stress states estimated from seismicity rate changes in the Tokai region, central Japan. *Tectonophysics*, 417:53–68, 2006.
- [82] Shinji Toda, R. S. Stein, K B Richards-Dinger, and Serkan B Bozkurt. Forecasting the evolution of seismicity in southern California: Animations built on earthquake stress transfer. *Journal of Geophys. Res.*, 110:B05S16, 2005.
- [83] Lisa A Wald, L Katherine Hutton, and Douglas D Given. The southern California Network bulletin: 1990-1993 summary. *SRL*, 66, 1995.
- [84] Lisa A Wald and Stan Scharwz. The 1999 Southern California Seismic Network bulletin. *SRL*, 71, 2000.
- [85] F Waldhauser, W L Ellsworth, and A Cole. Slip-parallel seismic lineations along the northern Hayward fault, California. *Geophys. Res. Lett.*, 26:3525–3528, 1999.

- [86] F Waldhauser and M Tolstoy. Seismogenic structure and processes associated with magma inflation and hydrothermal circulation beneath the East Pacific Rise at $9^{\circ}50'N$. *Gcubed*, 12:Q08T10, 2011.
- [87] Felix Waldhauser. hypodd - a program to compute double-difference hypocenter locations (hypodd version 1.0 - 03/2001). Open File Report 01-113, U.S. Geol. Survey, 345 Middlefield Rd, MS977 Menlo Park, Ca 94025, 2001.
- [88] Felix Waldhauser and William L Ellsworth. A double-difference earthquake location algorithm: Method and application to the Northern Hayward fault, California. *Bull. Seism. Soc. Am*, 90(6):1353–1368, 2000.
- [89] Shengji Wei, E Fielding, Sebastien Leprince, Anthony Sladen, J.-P. Avouac, D. V. Helmberger, E Hauksson, Mark Chu, Risheng and Simons, K W Hudnut, Thomas Herring, and Richard Briggs. Superficial simplicity of the 2010 El Mayor-Cucapah earthquake of Baja California in Mexico. *Nat. Geosci.*, 2011.
- [90] R J Weldon II, T E Fumal, T J Powers, S K Pezzopane, K M Scharer, and J C Hamilton. Structure and Earthquake Offset on the San Andreas Fault at the Wrightwood, California, Paleoseismic Site. *Bull. Seism. Soc. Am*, 92:2704–2725, 2002.
- [91] S. G. Wesnousky. Predicting the endpoint of earthquake ruptures. *Nature*, 444, 2006.
- [92] Robert L Wesson. Modelling aftershock migration and afterslip of the San Juan Bautista, California, earthquake of October 3, 1972. *Tectonophysics*, 144:215–229, 1987.

Accurate relocations are calculated in two steps: 1) determine differential times

of closely linked events from phase arrival and cross-correlation data through a preprocessing routine called *ph2dt* and 2) reduce the residuals between observed and calculated travel times for pairs of earthquakes at common stations by iteratively adjusting the vector distance between the event pair using the double-difference algorithm, *hypoDD*.

Appendix A

ph2dt

Ph2dt computes travel time differences between event pairs using traditional P- and S-wave phase arrivals and waveform cross-correlation delay times. This preprocessing step is necessary to determine linkage of events, eliminate redundancies in the data, and optimize the quality of data for use in *hypoDD*. Table 3a lists the parameters used in this step along with initial suggested values (italicized in Table 3b). *Ph2dt* creates a network of linked events using the nearest neighbors approach over a maximum search area (MAXSEP) until the maximum number of neighbors (MAXNGH) is reached. To be considered a strongly linked pair each event must have at least 8 links (MINLNK), where a link is an observation of a single P or S wave differential travel time or cross-correlation delay time (e.g. 4 stations recording both earthquakes P-wave arrival on the vertical component). In theory, there should be one link for every degree of freedom [i.e. three hypocentral parameters (x, y, and z) and origin time (t)] for two earthquakes totaling eight links, to maintain a stable system of equations. In practice, the system of equations remains well behaved with a MINLNK of four.

The size of the problem is pre-determined by increasing or decreasing the number of links per saved pair (MINOBS/MAXOBS). Since the number of delay times can

become very large (i.e. $>10^6$) even for a small number of events, it may be necessary to limit the number of links for an event pair by limiting the number of observations used. It is best to use a large number of MAXOBS (i.e. 50) when a limited number of stations is available; however, only considering strongly linked events (by setting MINOBS = MINLNK) may regulate the size of the problem for a large number of events. The number of calculations may also be limited with the MAXNGH parameter. Due to the nature of double-difference, the algorithm requires events to be closely spaced if they are to be used in the relocation, therefore each event can possibly have several hundred neighbors (depending on the number of events), resulting in millions of differential times, which become too cumbersome for hypoDD to manage. It is suggested to only use a relatively small number (i.e. MAXNGH ~ 10 , with MINOBS = 4 - 8) of strongly linked events. See the hypoDD manual for further details on ph2dt and the relationship of the input parameters [87].

Systematic tests were run, in which the above mentioned parameters were varied to seek minimum outliers and maximum delay times, neighbors, linked pairs, and number of events (Table 3b), while still maintaining computational efficiency for step 2. Tests with small MAXSEP (e.g. 2) and large MAXLNK/MAXNGH (e.g. 8 and 20, respectively) that returned $>10^6$ delay times were considered to be computationally inefficient, as the size of the problem became too large for hypoDD. Larger problems with limited numbers of links per pair (e.g. 2) tend to be ill-conditioned and unstable. The goal was to preserve as much data as possible, while still allowing the double-difference algorithm to effectively reduce residuals and produce accurate locations.

HypoDD

One goal of *hypoDD* is to incorporate multiple data types (e.g. catalog and cross-correlation delay times) in the relocation process, while still maintaining a well-conditioned system of equations and appropriate connectivity of events. This is achieved through two parameters, `OBSCCT` and `OBSCC`, the number of observations for each event pair using catalog data (phase delay times) and cross-correlation delay times, respectively. In general, this should equal the number of `MINLNKs` used in *ph2dt*, but no less than 8. Additionally, *hypoDD* allows for the implementation of re-weighting schemes defined specifically for each problem and data type. When using catalog and cross-correlation data, the initial iterations are controlled by the catalog data and are used to estimate the absolute location of the clusters. The latter iterations are primarily controlled by the cross-correlation data and are used to estimate the relative location between each event and its neighbors. Again, systematic tests were run in which the re-weighting scheme was varied until the maximum reduction in residuals, error estimates, and number of relocated events was found. Another important parameter, `DAMP`, is used when *hypoDD* solves the damped least-squares problem with the conjugate-gradient method (LSQR). This damping factor (`DAMP`) damps the hypocentral adjustments so they don't become too large or unstable. The `DAMP` value is strongly related to the condition of the system, expressed as the ratio of the largest to smallest eigenvalues in the condition number (CND). Well-conditioned systems have empirically derived CND and `DAMP` values between 40–80 and 1–100, respectively [87]. Our tests show the condition of the system is highly dependent upon the initial parameters used in *ph2dt*. Over-damping the solution causes hypocenters to collapse onto a single point, while under-damping causes event pair separation distances to increase by orders

of magnitude, and the absolute location of the cluster to shift 100s of km.

A second goal of *hypoDD* is to relocate earthquakes with minimal effects from unknown Earth structure. While a velocity model and P- and S-wave velocity ratio are required, the algorithm only accommodates a 1D layer-cake model. The number of layers (maximum $NLAY = 13$) was varied; which resulted in a decrease in location accuracy was seen with increasing $NLAY$, particularly when applying small steps in both velocity and depth. This is primarily due to over-constraining the depths by included too many layers in the velocity model. Additionally, the velocity nearest the surface was determined to be critically important. An overestimation of the wave speed in this layer overestimated the distance between the station and the earthquake, which resulted in a large number of ‘air-quakes’ (i.e. events that located above the free surface). Furthermore, inaccurate velocities and large steps in the 1D velocity model produce a similar effect. Events located above a velocity step tend to be pushed down, while events located below this boundary tend to be pushed up, which results in a clustering of seismicity right at the step- boundary that is clearly an artifact of the relocation procedure.

Appendix B

A 3D movie is attached as an electronic supplement to this work and can be found at: <https://dl.dropbox.com/u/13342712/YuhaDesert38-noplanes.avi>

Here, the final HDb locations are plotted as a function of density color. Eight clusters were identified using a Gaussian Mixture Model. The video begins in map view and rotates clockwise through 360 degrees at view elevations between 0 and 90 degrees. In this movie, it is possible to identify individual fault planes that remains as distinct structures at depth. These fault structures do not appear to coalesce onto simpler, through-going structures at depth.